PHYSICAL REVIEW B VOLUME 11, NUMBER 2 15 JANUARY 1975

Ground-state wave function for shallow-donor electrons in silicon. I. Isotropic electron-nuclear-double-resonance hyperfine interactions*

Jerry L. Ivey†
Aerospace Research Laboratories, Wright-Patterson Air Force Base, Ohio 45433

Robert L. Mieher
Department of Physics, Purdue University, West Lafayette, Indiana 47907

(Received 22 July 1974)

In a new theoretical investigation of electrons bound to the shallow-donor impurities (P, As, Sb) in silicon we have calculated the Fermi-contact hyperfine-interaction constants for the Si^{29} lattice nuclei surrounding the impurity nucleus. We have used a model potential which represents the impurity potential, a wave-vector-dependent dielectric function which represents the screening of the impurity potential by the silicon lattice, and pseudopotential Bloch functions for the calculation of the wave-function density of the $1s(A_1)$ ground state at the nuclear sites. The restrictions of the effective-mass theory to a single band and to conduction-band-minima Bloch functions have been removed because we represent the wave function in terms of a Bloch-function expansion throughout the Brillouin zone for several bands. With the use of the Fermi-contact constants calculated from this wave function, we have been able to make definite matchings of Si^{29} lattice sites and the electron-nuclear-double-resonance (ENDOR) shells measured by Hale and Mieher. With these matchings we are able to explain the experimentally observed lack of inversion symmetry of the electronic wave function and to explain most of the donor dependence of the experimental ENDOR data. Tutorial type discussions of the comparison of this calculation with effective-mass calculations are presented. These results contain several features that are due to the complex values of the wave-function expansion coefficients and the complex values of the Bloch functions; these features cannot be obtained from any real-valued effective-mass Hamiltonian.

I. INTRODUCTION

One of the fundamental problems of solid-state physics is the nature of impurities in a host-crystal lattice. The detailed first-principles calculations of the energy levels and the wave functions are always difficult. Therefore, various models and approximations are used in the theoretical calculations. Many properties of shallow impurity centers in semiconductors have been understood through the effective-mass model.[1] In fact, recent improvements[2] in the effective-mass treatment (EMT) have given excellent energy values for the excited states of the shallow donors. However, there are important problems for which the EMT has proven inadequate. The most critical test of a theoretical wave function is provided by the detailed hyperfine-interaction data obtained from the electron-nuclear-double-resonance (ENDOR) technique.[3,4] Unfortunately, the best predictions of the EMT, even with modifications to describe the donor-dependent "chemical shifts" of the donor ground-state energies, are not sufficiently accurate to permit interpretation of more than a few of the ENDOR lines observed for the shallow donors in silicon.[5]

The ENDOR data[3-5] can be analyzed in terms of an ENDOR spin Hamiltonian

$$\mathcal{H}_E = \sum_l \vec{I}_l \cdot (a_l \vec{S} + \overleftrightarrow{B}_l \cdot \vec{S} - g_n \mu_N \vec{H}_0), \tag{1}$$

where the index l refers to the lattice sites occupied by nuclei with magnetic moments, $\vec{I}_l$ is the nuclear spin, $\vec{S}$ is the unpaired electron spin, and the last term is the nuclear Zeeman interaction with the applied magnetic field. The term a_l represents the isotropic Fermi-contact hyperfine interaction and may be written

$$a_l = (\tfrac{8}{3}\pi) g g_n \mu_B \mu_N |\Psi(\vec{R}_l)|^2, \tag{2}$$

where $|\Psi(\vec{R}_l)|^2$ is the wave-function density at the nucleus located at the position $\vec{R}_l$ with respect to the donor site. The anisotropic part of the hyperfine interaction results from the dipole-dipole interaction between the magnetic moments of the unpaired donor electron and the lattice nucleus. This anisotropic interaction term may be written

$$(\overleftrightarrow{B}_l)_{ij} = g g_n \mu_B \mu_N \langle \Psi | (3x_i x_j - r^2 \delta_{ij}) / r^5 | \Psi \rangle, \tag{3}$$

where the integration is over all space and the value of the wave-function density $|\Psi(\vec{r})|^2$ at all points in space contributes to the $\overleftrightarrow{B}$ tensor.

The experimental value of a_l and $(\overleftrightarrow{B}_l)_{ij}$ for the Si^{29} nuclei for the shallow donors P, As, and Sb are tabulated in Ref. 4. Also, the variation of a_l

when a compressional uniaxial stress was applied along the [100] axis was studied by Hale and Castner.[6] From their measurements they were able to determine the piezohyperfine constants which described the stress dependence of a_l.

An ENDOR shell is composed of a group of equivalent lattice sites which have the same value of a_l, for example, the lattice sites $(0,0,4)$, $(0,0,\bar{4})$, $(0,4,0)$, $(0,\bar{4},0)$, $(4,0,0)$, and $(\bar{4},0,0)$ will be referred to as the $(0,0,4)$ shell. The experimental spectra of such a shell is made up of several lines whose angular anisotropy (as the crystal is rotated in the applied dc magnetic field) is described by the dipole-dipole constants $(\vec{B}_l)_{ij}$. There have previously been reported six attempts to match the experimentally determined ENDOR shells to shells of equivalent lattice sites. In the original ENDOR study of the shallow donors Feher[3] measured five shells which he labeled A, B, C, D, and E, and matched them to the $(0,0,4)$, $(4,4,0)$, $(\bar{3},\bar{3},\bar{3})$, $(5,5,5)$, and $(1,1,1)$ shells, respectively, on the basis of their a_l values. Hale and Mieher,[4] who reported improved measurements on these five shells and on some 17 additional shells, showed that the D-$(5,5,5)$ match was erroneous because of symmetry considerations but could add only the one additional match of K-$(0,0,8)$. An attempt by Hale and Mieher[7] to calculate the dipole-dipole constants $(\vec{B}_l)_{ij}$ failed to add any additional matchings. These three attempts to provide a theoretical explanation of the ENDOR results used the effective-mass approximation to represent the wave function $\Psi(\vec{r})$ by

$$\Psi(\vec{r}) = \left(\frac{1}{6}\right)^{1/2} \sum_{j=1}^{6} F_j(\vec{r})\psi_0(\vec{k}_{0j}, \vec{r}), \tag{4}$$

where the $F_j(\vec{r})$ are hydrogeniclike envelope functions derived from the effective-mass Hamiltonian and the $\psi_0(\vec{k}_{0j}, \vec{r})$ are Bloch functions of the conduction-band minima located at $\vec{k}_{0j}$ along the Δ axes of the Brillouin zone. Also, Hale and Castner[6] used the effective-mass approximation to calculate the theoretical piezohyperfine constants. By comparison of the theoretical and experimental piezohyperfine constants they could add only one definite matching of the Q-$(1,1,5)$ shell, although they did suggest several possible additional matchings.

Two more recent attempts to explain the ENDOR results were by Castner[8] and by Ning and Sah.[9] The first work attempted to admix wave-function components from the "subsidiary minima" at the L, K, and U points in the Brillouin zone. The second work considered intervalley overlap terms (the valley-orbit interaction) and calculated the ionization energies of the $1s(A_1)$, $1s(T_2)$, and $1s(E)$ states of the shallow donors in silicon. Using parameters determined by the fit of their variational envelope function to the energies, they then recalculated the Fermi-contact constants using Eq. (4). Neither the work of Castner[8] nor that of Ning and Sah[9] can be used to assign lattice sites to any additional ENDOR shells.

In this paper we report a new calculation[10] of the Fermi-contact constants. Instead of using the envelope-function approach as used in all previous work, we calculate the donor-electron wave function numerically as an expansion in Bloch functions throughout the Brillouin zone for several energy bands. We use a model impurity potential, the dielectric screening of the impurity potential, and the nature of the Bloch functions for all points in the Brillouin zone. Our new theoretical a_l values permit for the first time definitive assignments of experimental ENDOR lines to specific lattice sites in the silicon lattice. These new a_l values are more accurate than the EMT predictions and have only one-fifth as large a root-mean-square error as the EMT results; note, however, that it was not even possible to determine the accuracy of the EMT until the calculations reported here permitted the identification of the experimental shells.

In Sec. II we present the details of this calculation of the ground-state $1s(A_1)$ wave function and of the Fermi-contact constants. Section III contains the results of this calculation and a comparison of the theoretical and experimental Fermi contact constants. We continue in Sec. IV with a comparison of the results of the EMT approach and of the present work.

II. CALCULATION OF SHALLOW-DONOR WAVE FUNCTIONS

A. Use of pseudopotentials and model potentials

For an electron moving in a screened Coulomb potential one can write a pseudopotential equation[11,12]

$$[T + V_p(\vec{r}) + U_p^s(\vec{r})]\Psi_p(\vec{r}) = E\Psi_p(\vec{r}), \tag{5}$$

where T is the kinetic-energy operator, $V_p(\vec{r})$ is an appropriate periodic crystal potential,[13-15] and $U_p^s(\vec{r})$ is an appropriate pseudopotential for the screened impurity potential. Such a formalism has been used in practice by Faulkner[16] for isoelectronic impurities in GaP and by Callaway and Hughes[17] for the isolated vacancy in silicon. The unscreened impurity pseudopotential could in principle be calculated from the Hartree-Fock wave functions for the cores of silicon and the impurity. As discussed by Faulkner,[16] however, it is usually necessary to approximate such a pseudopotential by an analytic function so that one can perform the large number of mathematical operations which are necessary in order to solve an equation such as Eq. (5) in a reasonable amount of computer time. With this in mind we have assumed for the unscreened local model pseudopotential

$$\begin{aligned} U_p(r) &= -U_0\,, \quad r < r_m \\ &= -e^2/r, \quad r > r_m. \end{aligned} \tag{6}$$

The potential U_0 could be taken as the difference (within a suitable radius r_m) between the model potential values for the impurity ion and a silicon ion taken, for example, from the model potential theory work of Heine and Abarenkov[18] and of Animalu.[19] However, details such as the anisotropy of the impurity potential and the effects of lattice relaxation around the impurity probably contribute to the energy and are not included in this study. Therefore, the procedure that we follow is to use U_0 (taken to have the same model potential radius of 2 a.u. for each donor) to adjust the calculated ionization energies for the different donors to the experimental energy values.[20] This approach is similar to that used in the EMT work of Kohn and Luttinger,[1,21] where the experimental value of the ionization energy is introduced into the calculation of the electronic wave function by the use of the Whittaker function.

B. Impurity-potential screening

Since the dielectric function of the silicon lattice is known to have a spatial variation,[22-26] it is necessary to introduce a wave-vector-dependent dielectric function to screen the potential in Eq. (6). The screened potential is then given by

$$U_p^s(\vec{r}) = \frac{V^{1/2}}{(2\pi)^3} \int \frac{U_p(\vec{k})}{\epsilon(\vec{k})}\, e^{i\vec{k}\cdot\vec{r}}\, d\vec{k}. \tag{7}$$

The dielectric function $\epsilon(\vec{k})$ for silicon has been found to be very nearly isotropic. Nara and Morita[24] found that $\epsilon(\vec{k})$ could be approximated by

$$\frac{1}{\epsilon(k)} = \frac{Ak^2}{k^2+\alpha^2} + \frac{Bk^2}{k^2+\beta^2} + \frac{C\gamma^2}{k^2+\gamma^2}\,. \tag{8}$$

Another calculation of $\epsilon(\vec{k})$ by Walter and Cohen[26] differed somewhat for small $\vec{k}$ but was believed by them to be more accurate because of a better consideration of special properties of the pseudopotential Bloch functions for silicon. We have chosen to make a fit of the results of Walter and Cohen to the above expression [Eq. (8)] which is a convenient form for computational purposes. With this form one can fit a smooth curve to the average of the $\epsilon(\vec{k})$ values for the [100], [110], and [111] directions. Figure 1 shows the $\epsilon(\vec{k})$ used in this work.

The value of the low-temperature static dielectric constant was taken as $\epsilon(0) = 11.40$. A measurement by Salberg and Villa[27] gave the value of the refractive index $n = 3.417$, which yields the value $\epsilon = 11.68$. This value was quoted for room temperature. The temperature dependence of n as reported by Cardona, Paul, and Brooks[28] is

$$\frac{1}{n}\frac{dn}{dT} = (3.9 \pm 0.4)\times 10^{-5}\,{}^\circ\mathrm{C}^{-1}. \tag{9}$$

If one assumes the constancy of this logarithmic derivative for the extrapolation to helium temperatures and the room temperature value of $\epsilon = 11.68$, the calculated value for $T = 4\,^\circ\mathrm{K}$ is $\epsilon = 11.41 \pm 0.03$. This value is in agreement with the value $\epsilon = 11.40 \pm 0.05$ found by Faulkner[2] from the splitting of the $2p$ excited states of the shallow donors in silicon.

With the use of Eqs. (6)–(8) we can write an analytic expression for $U_p^s(R)$, where $R = r/a^*$ (the effective radius a^* will be defined in Sec. II D) and $K = ka^*$:

$$RU_p^s(R) = -[(U_0R_m)U_1(R) + (e^2/a^*)U_2(R)]\,, \tag{10a}$$

$$U_1(R) = \frac{2}{\pi}\int_0^\infty dK\,\frac{\sin KR}{\epsilon(K)} \times\left(\frac{\sin KR_m - KR_m\cos KR_m}{KR_m}\right), \tag{10b}$$

$$U_2(R) = \frac{2}{\pi}\int_0^\infty dK\,\frac{\sin KR}{\epsilon(K)}\,(\cos KR_m). \tag{10c}$$

The particular form of this expression in terms of a part linearly dependent upon the model well depth U_0 illustrates the motivation for the choice of the square-well potential.

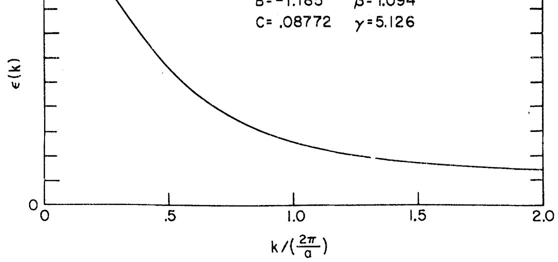

FIG. 1. Dielectric response function $\epsilon(k)$ used in this work. The value of $\epsilon(0)$ is taken as 11.4. The wave vector k is in units of $2\pi/a$, the value of the X point on the {100} Brillouin zone face.

C. Calculation of $A_n(\vec{k})$ $[E_n(\vec{k})-E]$

We now express $\Psi_p(\vec{r})$ in terms of the pseudopotential Bloch functions

$$\Psi_p(\vec{r}) = \sum_{n\vec{k}} A_n(\vec{k})\psi_n(\vec{k},\vec{r}). \tag{11}$$

By substitution of Eq. (11) into the Schrödinger equation (5), one can write

$$[E_n(\vec{k}) - E]A_n(\vec{k}) = -\int \psi_n^*(\vec{k},\vec{r})U_p^s(r)\Psi_p(\vec{r})\,d\vec{r}. \tag{12}$$

To solve this equation for $A_n(\vec{k})$ and E, for the potential $U_p^s(r)$ as given in Eq. (10), we represent $\Psi_p(\vec{r})$ for the evaluation of the right-hand side of Eq. (12) not by Eq. (11) but by the function

$$\Psi_p(\vec{r}) \to F(r)\Psi_c(\vec{r}), \tag{13}$$

where

$$\Psi_c(\vec{r}) = \left(\frac{V}{6}\right)^{1/2} \sum_{j=1}^{6} \psi_0(\vec{k}_{0j},\vec{r}) \tag{14}$$

is a sum over the pseudopotential functions for the six conduction-band minima and $F(r)$ is an appropriate envelope function (assumed in this work to be spherically symmetric). Substitution of Eqs. (13) and (14) into (12) then results in the equation

$$[E_n(\vec{k}) - E]A_n(\vec{k}) = -\int \psi_n^*(\vec{k},\vec{r})[U_p^s(r)F(r)]\,\Psi_c(\vec{r})\,d\vec{r}. \tag{15}$$

We define the Fourier transform of the product $U_p^s(r)F(r)$ as

$$W(\vec{k}) = \frac{1}{V^{1/2}} \int U_p(r)F(r)e^{-i\vec{k}\cdot\vec{r}}\,d\vec{r}. \tag{16}$$

With the use of Eqs. (7) for the Fourier transform of the screened potential function, we can also write this equation as

$$W(\vec{k}) = \frac{V^{1/2}}{(2\pi)^3} \int \frac{U_p(\vec{q})}{\epsilon(\vec{q})}\,a(\vec{k}-\vec{q})\,d\vec{q}, \tag{17}$$

where $a(\vec{k})$ is the Fourier transform of $F(r)$.

If we now express the pseudopotential Bloch functions in a series of reciprocal-lattice-vector plane waves

$$\psi_n(\vec{k},\vec{r}) = \frac{1}{V^{1/2}} \sum_{\vec{G}} b_n(\vec{k},\vec{G})e^{i(\vec{k}+\vec{G})\cdot\vec{r}}, \tag{18}$$

then the use of Eqs. (14), (17), and (18) allows us to write Eq. (15) as

$$\begin{aligned}[E_n(\vec{k}) - E]A_n(\vec{k}) = (-\tfrac{1}{6})^{1/2} &\sum_{j=1}^{6}\sum_{\vec{G},\vec{G}'} b_n^*(\vec{k},\vec{G}) \\ &\times b_0(\vec{k}_{0j},\vec{G}')W(\vec{k}_{0j}+\vec{G}'-\vec{k}-\vec{G}).\end{aligned} \tag{19}$$

The evaluation of the right-hand side of Eq. (19) is done only once for each of the terms in Eq. (10a). Equation (19) can now be written in the following form:

$$[E_n(\vec{k}) - E]A_n(\vec{k}) = -[(U_0R_m)Z_n^{(1)}(\vec{k}) + (e^2/a^*)Z_n^{(2)}(\vec{k})], \tag{20}$$

where

$$\begin{aligned}Z_n^{(i)}(\vec{k}) = 6^{-1/2}&\sum_{j=1}^{6}\sum_{\vec{G},\vec{G}'} b_n^*(\vec{k},\vec{G})b_0(\vec{k}_{0j},\vec{G}') \\ &\times W_i(\vec{k}_{0j}+\vec{G}'-\vec{k}-\vec{G})\end{aligned} \tag{21}$$

and

$$W_i(K) = -\left(\frac{4\pi}{V^{1/2}K}\right)\int_0^\infty RU_i(R)F(R)\sin KR\,dR. \tag{22}$$

It should be noted that care must be used in evaluating Eq. (10) because of the singularity at $R=R_m$. Both Eqs. (10b) and (10c) can be evaluated in closed form with the use of the formula in Eq. (8) for $1/\epsilon(k)$ for $R<R_m$ and $R>R_m$. The numerical evaluation of Eq. (22) must then be done separately in the two regions.

D. Discussion of the effective-mass theory and envelope functions

In the effective-mass theory the differential equation derivable[1] from Eq. (12) for a single conduction band with its minimum of energy at $\vec{k}=0$ is

$$[-(\hbar^2/2m^*)\nabla^2 + U_p^s(r) - E]\,F(r) = 0, \tag{23}$$

where

$$F(r) = V^{-1/2}\sum_{\vec{k}} A_0(\vec{k})e^{i\vec{k}\cdot\vec{r}}, \tag{24}$$

and Eq. (11) becomes

$$\Psi_p(\vec{r}) = \sum_{\vec{k}} A_0(\vec{k})\Psi_0(\vec{k},\vec{r}) = F(r)u_0(0,\vec{r}). \tag{25}$$

The subscript 0 denotes the lowest conduction band with an isotropic effective mass m^*. If $U_p^s(r)$ is taken as the Coulomb potential $(-e^2/\epsilon_0 r)$, the solution to Eq. (23) for $F(r)$ and E is

$$\begin{aligned}F(r) &= (1/\pi a^{*3})^{1/2}e^{-r/a^*}, \\ E^* &= -(e^2/2a^*\epsilon_0).\end{aligned} \tag{26}$$

The solution to Eq. (23) with the model potential of Eq. (6) screened by the static dielectric constant ϵ_0 is the Whittaker-function solution

$$F(r) = \begin{cases} A\sin Kr, & r \leqslant r_m \\ B\left(\dfrac{W(2r/\nu a^*)}{2r/\nu a^*}\right), & r \geqslant r_m \end{cases} \tag{27}$$

where

$$\nu = (E^*/E)^{1/2}.$$

The constants A, B, and K are determined by the matching of logarithmic derivatives at $r = r_m$ and by normalization.

When there are several equivalent conduction-band minima the EMT solution is a linear combination of the solutions of the individual minima. For the $1s(A_1)$ donor ground state in silicon the linear combination is given by Eq. (4). The $F_j(\vec{r})$ envelope functions in Eq. (4) are solutions of the anisotropic effective-mass Hamiltonian that is also derivable[1] from Eq. (12). This Hamiltonian for a k_z-axis minimum is

$$\left[-\frac{\hbar^2}{2m_l}\frac{\partial^2}{\partial z^2} - \frac{\hbar^2}{2m_t}\left(\frac{\partial^2}{\partial x^2} + \frac{\partial^2}{\partial y^2}\right) + U_p^s(r) - E\right] F_z(\vec{r}) = 0. \tag{28}$$

The standard EMT solution used for this equation is the variational function

$$F_z^v(\vec{r}) = (\pi a_l a_t^2)^{-1/2} \exp\{-[(x^2+y^2)/a_t^2 + z^2/a_l^2]^{1/2}\}, \tag{29}$$

and a_l, a_t, and E^* are now determined by variational procedures with $U_p^s(r)$ taken as the Coulomb potential $(-e^2/\epsilon_0 r)$. Then to correct for the fact that the $U_p^s(r)$ is more complicated than a Coulomb potential and that the experimental energies are not equal to E^* a composite anisotropic envelope function is used[1,3,5] of the form

$$F_z(\vec{r}) = F(r)\left(\frac{a^{*3}}{a_t^2 a_l}\right)^{1/2} \times \exp\left[-\left(\frac{x^2+y^2}{a_t^2} + \frac{z^2}{a_l^2}\right)^{1/2}\right] \Big/ \exp\left(\frac{-r}{a^*}\right), \tag{30}$$

where the isotropic $F(r)$ is the spherically symmetric Whittaker-function solution given by Eq. (27) and now E^* is the energy determined from the variational solution Eq. (29) and a^* is the isotropic effective radius that one would have with a Coulomb potential and an isotropic effective mass m^* that gave the variational energy E^*. The energy E in the expansion for ν in Eq. (27) is now taken as the experimental energy.

In this work we use for our starting envelope function in Eq. (16) only the spherically symmetric $F(r)$ given by Eq. (27) so that we need evaluate only one-dimensional Fourier transforms. However, our final results contain both the effective-mass-type anisotropies as well as other anisotropies that are not included at all in the EMT. We give a detailed comparison of the results of this work with the EMT results in Sec. IV.

In Eq. (27) we use the value of $E^* = 31.27$ meV from the work of Faulkner[2] which used the static dielectric constant value $\epsilon_0 = 11.40$. From Eq. (26) this gives $a^* = 20.2$ Å. The experimental energy values are taken from the work of Aggarwal and Ramdas[20] when corrected[2] for a value of $\epsilon_0 = 11.40$. These values are then 53.73, 45.53, and 42.73 meV for arsenic, phosphorus, and antimony donors, respectively.

Figure 2 shows the Whittaker function solution $F(r)$ for the phosphorus donor as curve 1. Also shown in Fig. 2 are plots of $F_z(\vec{r})$ for phosphorus as given by Eq. (30) along the z axis (curve 4) and perpendicular to the z axis (curve 3). [Our first calculations were made by approximating the Whittaker-function solution by two exponentials as reported in Ref. 10. This approach permitted an examination of how sensitive our results were to small changes in the $F(r)$ that is used in Eq. (16). Curve 2 is a two-exponential approximation given by Eq. (48) and will be discussed in Sec. III A.]

Figure 3 shows the Fourier transforms of the Whittaker-function solution (curve 1) and of the two-exponential approximation (curve 2). Also shown in Fig. 3 are curves 3 and 4 which correspond to the like-numbered curves in Fig. 2 except

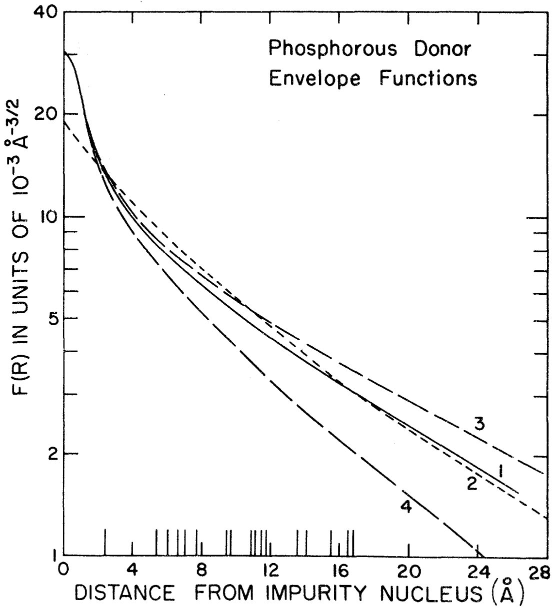

FIG. 2. Curve labeled (1) is the Whittaker function solution for the phosphorous donor. Curve (2) is a two-exponential function given by Eq. (48). Curve (4) is a plot along the z axis of $F_z(\vec{r})$ as given by Eq. (30). Curve (3) is a plot of $F_z(\vec{r})$ perpendicular to the z axis. The long marks located on the bottom scale line indicate the distances between the identified ENDOR nuclei and the donor site.

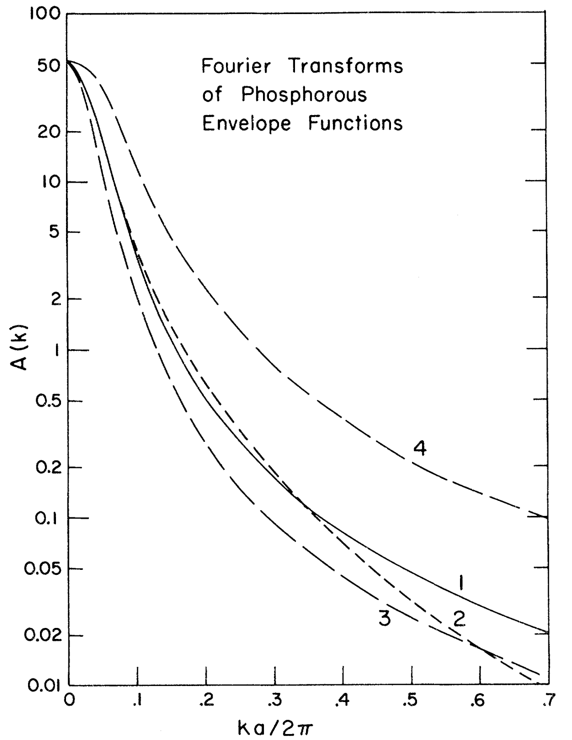

FIG. 3. Curve (1) is the Fourier transform of the Whittaker function solution $F(r)$ as given by Eq. (27) and curve (1) of Fig. 2. Curve (2) is the Fourier transform of the two-exponential curve (2) of Fig. 2. Curves (3) and (4) represent curve (1) multiplied by the ratio of the transform of the variational function of Eq. (30) to the transform of the exponential function, Eq. (26). Curve (4) is for a k-space direction parallel to the major axis of the effective-mass ellipsoid (the $m_{\parallel}$ direction) and curve (3) is for a perpendicular ($m_{\perp}$) direction. All curves have been multiplied by $1/\sqrt{6}$ so that the sum of $|A(\vec{k})|^2$ for all six conduction-band minima is normalized to unity within the Brillouin zone.

that they are the products of the Fourier transform of the Whittaker function with the Fourier transform of the anisotropic function, Eq. (29), divided by the transform of Eq. (30). This is not the Fourier transform of Eq. (30), but then Eq. (30) itself is a rather intuitive composite function. We use the composite Fourier transform only for purposes of comparison with our results.

E. Determination of the energy E

If the value of $k_0/k_{\max}$ is known ($k_{\max}=2\pi/a$ is the distance to the face of the first Brillouin zone along the Δ axis) so that one can use the correct pseudopotential Bloch functions $\psi_{n_0}(\vec{k}_{0j},\vec{r})$ corresponding to the six degenerate conduction-band minima, then the product $A_n(\vec{k})[E_n(\vec{k})-E]$ can be evaluated from Eq. (19) for any given values of $\vec{k}$ and U_0. We have used the most recent set of pseudopotential form factors for silicon suggested by Saravia and Brust.[15] These values are used in a computer program which uses the Löwdin method[29] to calculate the $b_n(\vec{k},\vec{G})$ for any value of $\vec{k}$ chosen. In this work we keep only the four valence and the lowest four conduction bands. The program was originally written by Brust[13] and later modified by Faulkner,[30] to whom we are indebted for his furnishing us a copy of this program.

Using these parameters in the Brust-Faulkner program, one finds that the value of k_0 is almost exactly on the common boundary of two boxes on a cubic mesh defined by the interval $\frac{1}{24}k_{\max}$ which is used by Saravia and Brust,[15] i.e., $k_0/k_{\max}=20.5/24=0.854$. Since this value is the same as the best previous value,[3,5,6,31] $k_0/k_{\max}=0.85\pm0.03$, we have used it as our initial choice. The next step is to determine a mesh of points in reciprocal space at which the $A_n(\vec{k})$ are to be calculated. This grid cannot be too fine because it takes approximately 30 sec of CDC 6500 time to calculate the $A_n(\vec{k})[E_n(\vec{k})-\vec{E}]$ for a single value of $\vec{k}$. If the grid is too coarse, however, the accuracy of the calculation of the wave function from the $A(\vec{k})$ will suffer. After some experimentation we have chosen 200 points in a modular wedge, which is $\frac{1}{48}$ the reduced zone of the diamond lattice and is defined by $k_x\geq k_y\geq k_z\geq 0$. Shown in Fig. 4 are the boundaries of this wedge in a (100) plane in reciprocal space. The first 120 of these points are defined by the interval $\frac{1}{24}k_{\max}$ and are in the neighborhood of k_0. They are defined by $k_{l,m,n}=\frac{1}{24}k_{\max}(l,m,n)$ with $17\leq l\leq 24$, $0\leq m\leq 4$, and $0\leq n\leq 4$ for the vicin-

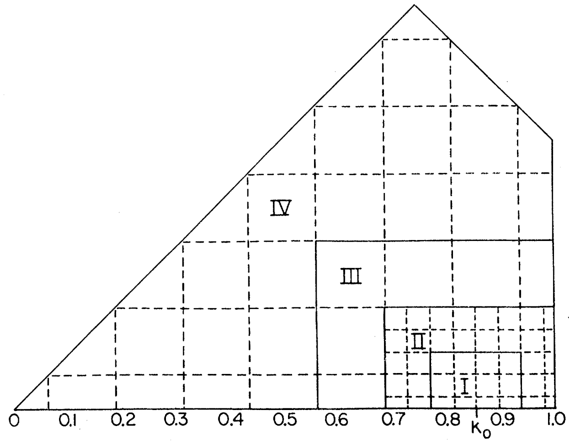

FIG. 4. (100) face of the modular wedge that has $\frac{1}{48}$th the volume of the Brillouin zone. The grid system used in the numerical calculations is indicated. The roman numerals label the different parts of the zone referred to in Fig. 5 and later figures.

ity of a $(+)k_x$ conduction-band minimum and are labeled as regions I and II in Fig. 4. The remaining 80 of these 200 points correspond to all the points defined by the interval $\frac{1}{8}k_{\max}$ which are in the modular wedge but not included in the first set and are labeled as regions III and IV in Fig. 4. Other points in the rest of the Brillouin zone can be obtained from these 200 points by group operations. An integration over the Brillouin zone [3645 boxes of size $\frac{1}{24}k_{\max}$ and 1913 boxes of size $\frac{1}{8}k_{\max}$] can now be reduced to a summation over these 200 points. Since $|A_n(\vec{k})|^2$ will be the same for all 48 points related by operations of the O_h^7 group of the diamond lattice,

$$\sum_{n,\vec{k}} |A_n(\vec{k})|^2 = \frac{V}{(2\pi)^3} \sum_{n,\vec{k}_i} |A_n(\vec{k}_i)|^2 V(\vec{k}_i) \frac{48}{C(\vec{k}_i)} , \tag{31}$$

where $V(\vec{k}_i)$ is the volume in k space of the grid box labeled by $\vec{k}_i$, $C(\vec{k}_i)$ for a given value of $\vec{k}_i$ is the number of regions (each $\frac{1}{48}$ the reduced zone) among which the point $\vec{k}_i$ is shared.[13]

We now summarize the steps used to calculate the $A_n(\vec{k})$ from Eq. (20): (i) determine the Whittaker function solution $F(r)$ of Eq. (27) that corresponds to the donor's experimental ionization energy; (ii) calculate the $W(k)$ of Eqs. (16) and (22) using the screened potential $U_p^s(r)$ of Eq. (10); (iii) determine the value of U_0 which ensures a normalized solution

$$\sum_{n,\vec{k}} |A_n(\vec{k})|^2 = 1$$

for E equal to the experimental ionization energy.

F. Calculation of $|\Psi(\vec{R}_l)|^2$ and a_l

The pseudopotential wave function of the donor electron is given by

$$\Psi_p(\vec{r}) = \sum_{n,\vec{k}} A_n(\vec{k})\psi_n(\vec{k}, \vec{r}) = \frac{1}{V^{1/2}} \sum_{n,\vec{k}} A_n(\vec{k}) u_n(\vec{k}, \vec{r}) e^{i\vec{k}\cdot\vec{r}} . \tag{32}$$

An evaluation of this expression can be facilitated by a consideration of the O_h^7 group of the diamond lattice. As discussed by Faulkner[16] the phases of the Bloch functions can be chosen such that $\psi_n(\vec{k}, 0)$ is real and positive. This choice of phase of the Bloch functions ensures that

$$\{\alpha\}|n\vec{k}) = |n\alpha\vec{k}),\ \psi_n(-\vec{k}, \vec{r}) = \psi_n^*(\vec{k}, \vec{r}); \tag{33}$$

$$A_n(\alpha\vec{k}) = A_n(\vec{k}),\ A_n(-\vec{k}) = A_n^*(\vec{k}); \tag{34}$$

$$u_n(\alpha\vec{k}, \vec{R}_l) = u_n(\vec{k}, \vec{R}_l),\ u_n(-\vec{k}, \vec{R}_l) = u_n^*(\vec{k}, \vec{R}_l); \tag{35}$$

where $\{\alpha\}$ denotes one of the 24 operations of the group T_d. The evaluation of Eq. (32) at a lattice site $\vec{R}_l$ can now be written

$$\Psi_p(\vec{R}_l) = \frac{V^{1/2}}{\pi^3} \sum_{n,\vec{k}_i} \frac{V(\vec{k}_i)}{C(\vec{k}_i)} \times \mathrm{Re}[A_n(\vec{k}_i) u_n(\vec{k}_i, \vec{R}_l) T(\vec{k}_i, \vec{R}_l)] , \tag{36}$$

where $\vec{k}_i$ is a point within the modular wedge (discussed in Sec. II E) which is $\frac{1}{48}$ the Brillouin zone and

$$\begin{aligned} T(\vec{k}_i, \vec{R}_l) = \tfrac{1}{4} \sum_{\{\alpha\}} e^{i\alpha\vec{k}\cdot\vec{R}_l} &= \{\cos k_x X(\cos k_y Y \cos k_z Z + \cos k_z Y \cos k_y Z) \\ &\quad - i[\sin k_x X(\sin k_y Y \sin k_z Z + \sin k_z Y \sin k_y Z)]\} \\ &\quad + \{\cos k_x Y(\cos k_y Z \cos k_z X + \cos k_z Z \cos k_y X) \\ &\quad - i[\sin k_x Y(\sin k_y Z \sin k_z X + \sin k_z Z \sin k_y X)]\} \\ &\quad + \{\cos k_x Z(\cos k_y X \cos k_z Y + \cos k_z X \cos k_y Y) \\ &\quad - i[\sin k_x Z(\sin k_y X \sin k_z Y + \sin k_z X \sin k_y Y)]\} , \end{aligned} \tag{37}$$

where we have left the l subscripts off the X_l, Y_l, Z_l site designations.

The grid of $\vec{k}$ values for this work has been chosen so that the variation of $A_n(\vec{k})$ and $u_n(\vec{k}, \vec{R}_l)$ from one grid point to the next should not introduce an appreciable error into the calculation. For large values of R_l, however, the exponential $e^{i\vec{k}_i\cdot\vec{R}_l}$ may be more rapidly varying than the other terms. To take into consideration the variation of the exponential across the volume $V(\vec{k}_i)$, each factor $e^{i\vec{k}_i\cdot\vec{R}_l}$ is multiplied by its average value across the volume:

$$J(\vec{k}_i, \vec{R}_l) = j_0(\tfrac{1}{2}x_l\Delta_i) j_0(\tfrac{1}{2}y_l\Delta_i) j_0(\tfrac{1}{2}z_l\Delta_i) . \tag{38}$$

In this expression $j_0(z) = z^{-1}\sin z$ and either $\Delta_i = \frac{1}{24}k_{\max}$ or $\Delta_i = \frac{1}{8}k_{\max}$ is the length of a cube edge. If one inserts Eq. (38) into Eq. (36), then the result is

$$\Psi_p(\vec{R}_l) = \frac{V^{1/2}}{\pi^3} \sum_{n,\vec{k}_i} \frac{V(\vec{k}_i)}{C(\vec{k}_i)} J(\vec{k}_i, \vec{R}_l) \times \mathrm{Re}[A_n(\vec{k}_i) u_n(\vec{k}_i, \vec{R}_l) T(\vec{k}_i, \vec{R}_l)] . \tag{39}$$

To relate this pseudopotential function to the experimentally determined Fermi-contact constants one must relate $|\Psi_p(\vec{R}_l)|^2$ to $|\Psi(\vec{R}_l)|^2$. To this end let us write for the "true" or orthogonalized wave function

$$\Psi(\vec{R}_l) = V^{-1/2} \sum_{n,\vec{k}} A_n(\vec{k}) u_n^0(\vec{k}, \vec{R}_l) e^{i\vec{k}\cdot\vec{R}_l}$$

or

$$\Psi(\vec{R}_l)=\frac{u_0^0(\vec{k}_0,\vec{R}_l)}{V^{1/2}}\sum_{n,k}A_n(\vec{k})\times\frac{u_n^0(\vec{k},\vec{R}_l)}{u_0^0(\vec{k}_0,\vec{R}_l)}\,e^{i\vec{k}\cdot\vec{R}_l}\,. \qquad (40)$$

Because of the considerable computer time required to obtain accurate expressions for $u_n^0(\vec{k},\vec{r})$, even if one has accurate pseudopotential functions $u_n(\vec{k},\vec{r})$ and core wave functions $\varphi_t(\vec{r})$, we have attempted to circumvent the evaluation of Eq. (40). We have used Hartree-Fock wave functions[32] for the silicon core states to calculate the ratio $u_n^0(\vec{k},\vec{R}_l)/u_0^0(\vec{k}_0,\vec{R}_l)$. We have found that for the two lowest conduction bands, the ratio can be accurately represented by the ratio of pseudopotential Bloch functions $u_n(\vec{k},\vec{R}_l)/u_0(\vec{k}_0,\vec{R}_l)$. For the other bands the accuracy of this ratio is less, but the contributions of the other bands to the isotropic hyperfine constants are small enough that the errors in using this ratio are unimportant. Therefore, we use the ratio of the pseudopotential functions, which enables us to express Eq. (40) as

$$\Psi(\vec{R}_l)=[u_0^0(\vec{k}_0,\vec{R}_l)/u_0(\vec{k}_0,\vec{R}_l)]\Psi_p(\vec{R}_l) \qquad (41)$$

and the Fermi-contact constants as

$$a_l=(\tfrac{8}{3}\pi)gg_n\mu_B\mu_N|u_0^0(\vec{k}_0,\vec{R}_l)/u_0(\vec{k}_0,\vec{R}_l)|^2\Psi_p\vec{R}_l)|^2\,. \qquad (42)$$

The value of $\eta\equiv|u_0^0(\vec{k}_0,\vec{R}_l)|^2$ has been obtained experimentally by Shulman and Wyluda[33] from measurements of spin-lattice relaxation times of Si^{29} nuclei interacting with conduction-band electrons. Their value of $\eta=186\pm18$ was later corrected to $\eta=178$ by Solomon as reported by Wilson.[34]

The a_l values obtained from Eq. (42) are listed in Table I along with the experimental a_l and the a_l values predicted by EMT.

G. Some additional convergence considerations

It was discussed in Sec. II E that 200 points in $\frac{1}{48}$ of the Brillouin zone were used in this calculation. Some convergence effects were examined by carrying out the numerical evaluation in $\vec{k}$ space [Eq. (40)] for an $A_n(\vec{k})$ determined by the Fourier transform of the two exponential approximation for the starting envelope function. This approximation is shown as line 2 in Figs. 2 and 3. Since this $A_n(\vec{k})$ could be quickly calculated, this had the advantage of permitting very fine grids to be used to check the dependence of the numerical summation on grid size. Several combinations of grid sizes were examined. When the results (for one band) of the summation of 200 points and of 3800 points in $\frac{1}{48}$ of the Brillouin zone (3^3 or 27 times as many total grid points in the entire zone for a total of about 150 000) were compared the calculated a_l values were larger by various amounts between 0% and 8%. Since an average change of about 4% could not be distinguished from an uncertainty in η, we can say that our numerical accuracy is about ±4%. Since this is about one half as large as our average error, we can say that limitations of numerical accuracy to using the 200 points probably contributes to the remaining discrepancies between theory and experiment, but it is not the only contributing factor, i.e., our numerical accuracy is consistent with the accuracy of the various physical approximations of this work. It should be noted, since this grid size convergence examination was made for $A_n(\vec{k})$ real valued and $u_n(\vec{k},\vec{R}_l)$ real and constant, that the convergence details are not necessarily the same as if the entire calculation were repeated for the 3800 grid points. We looked for any systematic relation between this numerical convergence examination and the remaining discrepancies between theory and experiment but we found none.

Figure 5 illustrates another convergence feature of the $\vec{k}$-space summation for the case of 3800 points in $\frac{1}{48}$ of the Brillouin zone. Different regions of the Brillouin zone around the conduction-band minima are labeled with Roman numerals in Fig. 4. The contact interactions resulting from limiting the sum in Eq. (24) to these different regions, with $A_0(k)$ given by curve 2 of Fig. 3, are shown in Fig. 5. This gives one an idea of the contributions of the different regions of $\vec{k}$ space. The column of values in Fig. 5 labeled $F(r)$ results from evaluating the analytic $F(r)$ as given in Eq. (48). The change between the last two columns of Fig. 5 illustrates that the contributions of $\vec{k}$ space outside the first zone are important in the summation in Eq. (24). One observes that contributions to the summation from all parts of the Brillouin zone are important for the first conduction band and that contributions from the rest of $\vec{k}$ space (which would come mostly from the second conduction band) are also important.

Although a finer grid in $\vec{k}$ space will probably be necessary if future calculations are to obtain better results than we report here, there is probably a more serious problem of numerical accuracy in this work. It is not possible to estimate just how much our results would change if we could reiterate our solution, i.e., take our calculated $A_n(\vec{k})$ and recalculate Eq. (12) using Eq. (11) instead of Eq. (13). To do this in a straightforward manner would require about three orders of magnitude more computer time than to do the work we report here.

TABLE I. Calculated[a] and experimental values of isotropic hyperfine constants and strain i.d. parameters.

Shell		Expt[b] $\frac{1}{2}a$	EMT[c] $\frac{1}{2}a$	I-M[d] $\frac{1}{2}a$	$G=0$ $\frac{1}{2}a$	$G=F^I=0$ $\frac{1}{2}a$	2Exp[e] $\frac{1}{2}a$	Expt[f] i.d.	EMT[g] i.d.	I-M i.d.
A-(0,0,4)	As	3860	5700	3803	3693	4646	4135	−0.129	−0.206	−0.264
	P	2981	4207	2924	2877	3364	3249	−0.178	−0.202	−0.233
	Sb	3101	3662	2554	2528	2850	3042	−0.143	−0.200	−0.217
B-(4,4,0)	As	3000	2237	2701	2718	2318	2799	0.124	0.243	0.170
	P	2254	1792	1922	1935	1715	2029	0.199	0.238	0.177
	Sb	1833	1616	1609	1621	1468	1758	0.147	0.236	0.181
C-(3,3,$\bar{3}$)	As	2037	1804	1991	1908	636	2114	0.0	0.0	0.0
	P	1649	1424	1477	1441	642	1602	0.0	0.0	0.0
	Sb	1397	1275	1267	1245	631	1455	0.0	0.0	0.0
D-(3,3,$\bar{7}$)	As	1292	1016	1242	1107	740	1290	0.044	0.061	−0.012
	P	1117	902	1008	933	682	1072	0.038	0.069	0.022
	Sb	1003	848	901	843	646	998	0.064	0.072	0.039
E-(1,1,1)	As	642	1212	3	0	330	⋯	0.0	0.0	0.0
	P	270	762	18	25	239	⋯	0.0	0.0	0.0
	Sb	293	616	45	51	202	⋯	0.0	0.0	0.0
F-(3,3,1)	As	1121	645	1295	1287	507	1278	−0.418	−0.876	−0.343
	P	840	494	788	787	378	786	−0.488	−0.872	−0.439
	Sb	504	436	606	611	327	609	−0.610	−0.871	−0.497
G-(7,7,$\bar{3}$)	As	806	771	861	831	650	888	−0.030	−0.069	−0.006
	P	764	734	774	755	622	818	−0.024	−0.075	−0.026
	Sb	761	709	725	712	600	794	−0.048	−0.077	−0.035
H-(4,4,$\bar{4}$)	As	801	962	943	895	805	1028	0.0	0.0	0.0
	P	689	816	787	762	683	873	0.0	0.0	0.0
	Sb	703	753	713	701	626	832	0.0	0.0	0.0
I-(2,2,$\bar{8}$)	As	718	975	646	672	694	678	−0.406	−0.367	−0.400
	P	685	858	589	605	621	635	−0.340	−0.363	−0.388
	Sb	643	804	556	563	578	627	−0.248	−0.362	−0.383
J-(5,5,5)	As	694	1321	657	668	1034	690	0.0	0.0	0.0
	P	739	1190	686	693	943	741	0.0	0.0	0.0
	Sb	761	1126	685	688	887	772	0.0	0.0	0.0
K-(0,0,8)	As	758	1017	649	627	518	688	−0.506	−0.636	−0.559
	P	663	865	570	557	488	621	−0.681	−0.641	−0.595
	Sb	629	802	529	519	466	607	⋯	−0.643	−0.611
L-(2,2,4)	As	741	976	716	837	730	763	−0.594	−1.129	−1.202
	P	582	746	537	600	555	584	−1.203	−1.139	−1.216
	Sb	525	660	462	502	479	529	⋯	−1.143	−1.224
M-(2,2,$\bar{4}$)	As	777	976	819	957	778	855	−0.949	−1.129	−1.175
	P	612	746	612	686	590	657	−1.210	−1.139	−1.190
	Sb	559	660	528	576	510	607	−0.797	−1.143	−1.196
N-(7,7,$\bar{7}$)	As	607	654	647	721	746	659	0.0	0.0	0.0
	P	612	654	634	679	696	664	0.0	0.0	0.0
	Sb	629	645	617	647	661	666	0.0	0.0	0.0
O-(4,4,4)	As	739	962	775	704	765	816	0.0	0.0	0.0
	P	598	816	652	598	654	703	0.0	0.0	0.0
	Sb	670	753	593	566	598	666	0.0	0.0	0.0
P-(2,2,8)	As	696	975	627	651	710	655	−0.280	−0.367	−0.382
	P	662	858	573	587	633	615	−0.330	−0.363	−0.371
	Sb	629	804	541	548	590	606	−0.235	−0.362	−0.365

TABLE I. *(Continued)*

Shell	Expt[b] $\frac{1}{2}a$	EMT[c] $\frac{1}{2}a$	I-M[d] $\frac{1}{2}a$	$G=0$ $\frac{1}{2}a$	$G=F^I=0$ $\frac{1}{2}a$	Expt[e] $\frac{1}{2}a$	Expt[f] i.d.	EMT[g] i.d.	I-M i.d.
Q-(1, 1, 5) As	566	817	545	642	828	574	0.428	0.412	0.587
P	524	651	447	498	601	483	0.486	0.419	0.560
Sb	387	585	403	435	508	457	0.576	0.422	0.547
R-(7, 7, 1) As	428	300	449	419	236	453	−0.488	−0.773	−0.325
P	379	288	378	361	237	391	−0.672	−0.765	−0.418
Sb	332	280	344	332	233	363	−0.511	−0.762	−0.461
S-(2, 2, $\overline{12}$) As	377	593	411	398	419	413	⋯	−0.178	−0.064
P	410	587	424	416	429	440	0.02	−0.165	−0.068
Sb	425	576	422	415	425	447	⋯	−0.160	−0.069
T-(2, 2, 12) As	364	593	401	388	430	402	⋯	−0.178	−0.054
P	398	587	415	407	439	429	0.01	−0.165	−0.059
Sb	425	576	412	406	434	436	⋯	−0.160	−0.160
U-(5, 5, 9) As	338	652	396	405	477	398	⋯	−0.098	0.044
P	383	637	424	432	486	442	−0.102	−0.091	0.015
Sb	425	622	428	433	479	458	⋯	−0.089	0.003
X-(5, 5, 1) As	242	1055	337	345	704	374	⋯	−0.300	−0.827
P	317	907	398	403	646	453	−0.6[h]	−0.303	−0.636
Sb	437	841	418	421	612	506	−0.4[h]	−0.304	−0.566
Δ (rms)%		60.8	11.2	12.5	38.8	13.0			

[a] All calculated values are for $k_0/k_{\max} = 0.854$; $\eta = 178$, and $\epsilon_0 = 11.4$.

[b] Data from Ref. 4.

[c] Calculated as in Ref. 5 of Hale and Mieher but for slightly different values of several parameters as discussed in Sec. II of this paper.

[d] This work.

[e] Calculated using the two exponential approximation for $F(r)$ as given in Eq. (48).

[f] Data from Ref. 6.

[g] Calculated values of i.d. parameter are obtained as discussed in the references of Hale and Castner.

[h] See discussion in Sec. III C5.

H. Dependence of calculation upon k_0

Any attempt to calculate Fermi-contact constants for a multivalley semiconductor must take into consideration the location of the conduction-band minima in the Brillouin zone. For silicon the exact location[31] of these minima along the Δ axis has not been determined by any experimental measurement with a precision such that the uncertainty has a negligible effect upon theoretical calculations of the contact interactions. In the present work the use of the Saravia-Brust[15] pseudopotential parameters gives a specific value of $k_0/k_{\max} = 0.854$. To attempt a completely consistent treatment of this question one should vary the pseudopotential parameters so as to change the location of the conduction-band minima (while keeping the effective-mass parameters fixed) and repeat the calculation of the Fermi-contact values. Such a procedure would use the ENDOR data in the same manner that the reflectivity data were used[13,15] to determine the pseudopotential parameters. At this time, however, this procedure would require far too much computer time and the over-all accuracy of the calculation is not yet good enough to justify such an approach. Therefore, we hoped that the value $k_0/k_{\max} = 0.854$ might be accurate enough to justify some type of interpolation procedure. Such a procedure should account for the k_0 dependence of interference effects caused by the six conduction-band minima and should yield the results of the EMT as one considers reducing the more complete theory back to the EMT.

The form of $a_l^{\mathrm{EMT}}(k_0)$ obtained from Eqs. (2), (4), and (30) is

$$a_l^{\mathrm{EMT}}(k_0) = A_0[F_x(\vec{R}_l)\cos k_0 x_l + F_y(\vec{R}_l)\cos k_0 y_l + F_z(\vec{R}_l)\cos k_0 z_l]^2 . \quad (43)$$

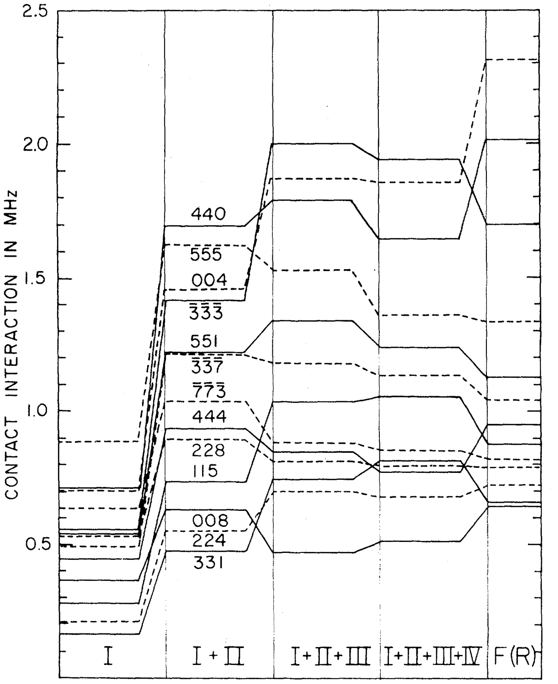

FIG. 5. Summary of the results of a convergence investigation of the contributions to the numerically evaluated hyperfine interactions from different regions of k space. The roman numerals refer to the regions so labeled in Fig. 4. These results refer to a spherically symmetric $A(k)$ as given by curve 2 in Fig. 3. The column labeled $F(r)$ results from the analytic $F(r)$ as given in Eq. (48). A very fine grid was used in this evaluation. The grid had each cube edge one third as long as those shown in Fig. 4 (i.e., 27 times as many grid points).

Since the interference effects among the six conduction-band minima have a pronounced effect upon the Fermi-contact values, it was felt that any interpolation procedure should be applied to an individual term such as $F_x(\vec{R}_l)\cos k_0 x_l$. Therefore, we defined an "interpolation envelope function" F_j^C as

$$F_j^C e^{i\vec{k}_{0j}\cdot\vec{r}} = \int_j A(\vec{k})\left(\frac{u(\vec{k},\vec{r})}{u(\vec{k}_{0j},\vec{r})}\right) e^{i\vec{k}\cdot\vec{r}}\,d\vec{k} \,. \tag{44}$$

The symbol $\int_j$ means that the integration is over the one sixth of extended $\vec{k}$ space associated with the jth conduction-band minimum. The boundaries between the six regions of $\vec{k}$ space are the $\{110\}$ planes. Due to the approximate nature of this approach the integration was limited to the first two conduction bands, i.e., the first two Brillouin zones in an extended-zone representation (see Fig. 2.19 on p. 116 of Ref. 35). For the other six bands we define

$$G_j^C(\vec{r}) = \sum_n{}' \int_j A_n(\vec{k})\left(\frac{u_n(\vec{k},\vec{r})}{u_0(\vec{k}_{0j},\vec{r})}\right) e^{i\vec{k}\cdot\vec{r}}\,d\vec{k} \,, \tag{45}$$

where the prime on the summation indicates that the sum over n excludes the lowest conduction bands, $n=5$ and 6. Since $A(\vec{k})$ and $u(\vec{k},\vec{r})$ are in general complex, the F_j^C and $G_j^C(\vec{R}_l)$ resulting from Eqs. (44) and (45) are also complex. In the effective-mass theory the variations in $u(\vec{k},\vec{r})$ are neglected and $A(\vec{k})$ is real-valued and sharply peaked about $\vec{k}_{0j}$ so that Eq. (44) becomes an identity and F_j is the real solution of the effective-mass Hamiltonian and all $G_j=0$.

Equations (44) and (45) were evaluated for each of the lattice sites, $r=R_l$, using $A_n(\vec{k})$ from Eq. (20). Since F_j^C is complex, Eq. (43) is replaced by

$$\begin{aligned} a_l(k_0) = A_0[&F_x^R(\vec{R}_l)\cos k_0x_l - F_x^I(\vec{R}_l)\sin k_0x_l + F_y^R(\vec{R}_l)\cos k_0y_l \\ &- F_y^I(\vec{R}_l)\sin k_0y_l + F_z^R(\vec{R}_l)\cos k_0z_l - F_z^I(\vec{R}_l)\sin k_0z_l \\ &+ G_x^R(\vec{R}_l) + G_y^R(\vec{R}_l) + G_z^R(\vec{R}_l)]^2 \,, \end{aligned} \tag{46}$$

where F_j^R and F_j^I are the real and imaginary parts of F_j^C. In other words, we assume that if k_0 in silicon is slightly different than $0.854k_{\max}$, then Eq. (46) will approximate the changed contribution of bands 5 and 6 while the smaller contributions of the other bands are assumed independent of small changes in k_0. The calculated values of F_j^C and G_j^C for the different lattice sites are tabulated in Table II as (F_j^R, F_j^I) and (G_j^R, G_j^I) and compared with the corresponding real F_j of the EMT. If the value $k_0=0.854\,k_{\max}$ is used, then Eq. (46) gives exactly the same results as Eq. (42). It should be emphasized that the F_j^C from Eq. (44) was used only for the purpose of examining the effects of a variation in k_0 from the value of $0.854\,k_{\max}$. It is not an integral part of the calculations that we are reporting here and, indeed, probably would not have been evaluated had the position of k_0 been exactly known. On the other hand, whatever reservations one may have about the meaning of this complex envelope function F_j^C it is presumably more meaningful than the widely used real effective-mass envelope function because Eq. (46) gives better agreement with the experimental data. Also, the evaluation of F_j^C permits some interesting comparisons with EMT.

III. COMPARISON OF THEORY AND EXPERIMENT

A. Theoretical values of a_l

The first column of numbers in Table I gives the experimental[4] a_l values. The second column of numbers gives the a_l values predicted by the EMT from Eqs. (30) and (43). The third column of

TABLE II. Comparison of calculated values of envelope functions.[a]

Shell	EMT F_x	EMT F_z	I-M[b] F_x	I-M F_z	I-M G_x	I-M G_z
A-(0, 0, 4) As	10.86	8.70	(10.01, 0.0)	(7.20, −3.33)	(−0.70, 0.0)	(1.72, 1.91)
P	9.30	7.58	(8.39, 0.0)	(6.55, −1.97)	(−0.44, 0.0)	(1.02, 1.17)
Sb	8.67	7.11	(7.66, 0.0)	(6.23, −1.40)	(−0.32, 0.0)	(0.73, 0.86)
B-(4, 4, 0) As	7.02	8.39	(7.42, 0.90)	(8.21, −0.61)	(−0.08, 0.07)	(0.11, 0.04)
P	6.33	7.45	(6.41, 0.58)	(7.03, −0.52)	(−0.06, 0.05)	(0.06, 0.04)
Sb	6.02	7.06	(5.94, 0.44)	(6.49, −0.49)	(−0.05, 0.04)	(0.04, 0.03)
C-(3, 3, $\bar{3}$) As	7.99	7.99	(4.74, −2.85)	(4.74, 2.85)	(−0.11, −0.10)	(−0.11, 0.10)
P	7.10	7.10	(4.76, −1.95)	(4.76, 1.95)	(−0.06, −0.06)	(−0.06, 0.06)
Sb	6.72	6.72	(4.72, −1.57)	(4.72, 1.57)	(−0.04, −0.05)	(−0.04, 0.05)
D-(3, 3, $\bar{7}$) As	5.63	4.27	(4.48, −1.44)	(4.05, 1.46)	(−0.31, −0.08)	(−0.11, 0.20)
P	5.26	4.08	(4.27, −1.05)	(3.93, 1.06)	(−0.18, −0.05)	(−0.07, 0.12)
Sb	5.08	3.98	(4.14, −0.39)	(3.84, 0.88)	(−0.13, −0.03)	(−0.05, 0.08)
E-(1, 1, 1) As	18.29	18.29	(9.54, 2.25)	(9.54, 2.25)	(−0.17, −0.38)	(−0.17, −0.38)
P	14.50	14.50	(8.11, 1.28)	(8.11, 1.28)	(−0.09, −0.22)	(−0.09, −0.22)
Sb	13.04	13.04	(7.46, 0.87)	(7.46, 0.87)	(−0.05, −0.15)	(−0.05, −0.15)
F-(3, 3, 1) As	8.96	10.04	(8.23, −0.67)	(10.54, 3.85)	(−0.03, 0.16)	(0.02, −0.07)
P	7.82	8.69	(7.00, −0.47)	(8.49, 2.42)	(−0.02, 0.11)	(0.02, −0.04)
Sb	7.35	8.13	(6.44, −0.39)	(7.59, 1.82)	(−0.01, 0.09)	(0.03, −0.03)
G-(7, 7, $\bar{3}$) As	3.55	4.50	(3.61, −1.72)	(3.01, 1.70)	(0.03, −0.06)	(−0.24, −0.09)
P	3.48	4.33	(3.46, −1.20)	(3.17, 1.28)	(0.02, −0.03)	(−0.15, −0.06)
Sb	3.42	4.24	(3.37, −0.98)	(3.20, 1.10)	(0.01, −0.02)	(−0.11, −0.04)
H-(4, 4, $\bar{4}$) As	6.08	6.08	(5.57, 0.23)	(5.57, −0.23)	(0.09, −0.26)	(0.09, 0.26)
P	5.60	5.60	(5.13, 0.22)	(5.13, −0.22)	(0.05, −0.16)	(0.05, 0.16)
Sb	5.38	5.38	(4.91, 0.22)	(4.91, −0.22)	(0.02, −0.11)	(0.02, 0.11)
I-(2, 2, $\bar{8}$) As	5.68	3.83	(4.63, 0.48)	(4.32, −0.60)	(0.12, −0.03)	(−0.07, −0.66)
P	5.31	3.69	(4.39, 0.35)	(4.01, −0.44)	(0.07, −0.01)	(−0.04, −0.40)
Sb	5.14	3.61	(4.24, 0.29)	(3.84, −0.38)	(0.05, −0.01)	(−0.03, −0.29)
J-(5, 5, 5) As	4.76	4.76	(4.21, 1.83)	(4.21, 1.83)	(−0.02, −0.19)	(−0.02, −0.19)
P	4.52	4.52	(4.02, 1.27)	(4.02, 1.27)	(−0.01, −0.11)	(−0.01, −0.11)
Sb	4.40	4.40	(3.90, 1.03)	(3.90, 1.03)	(−0.01, −0.08)	(−0.01, −0.08)
K-(0, 0, 8) As	6.22	3.99	(4.65, 0.0)	(4.41, 0.84)	(0.09, 0.0)	(−0.03, 0.38)
P	5.76	3.83	(4.49, 0.0)	(4.12, 0.56)	(0.06, 0.0)	(−0.01, 0.22)
Sb	5.55	3.73	(4.38, 0.0)	(3.96, 0.44)	(0.04, 0.0)	(−0.01, 0.15)
L-(2, 2, 4) As	8.85	7.70	(7.81, 0.27)	(7.13, −0.56)	(0.10, −0.18)	(0.58, 0.50)
P	7.77	6.84	(6.85, 0.10)	(6.34, −0.31)	(0.06, −0.12)	(0.34, 0.31)
Sb	7.32	6.47	(6.39, 0.03)	(5.96, −0.20)	(0.04, −0.09)	(0.24, 0.23)
M-(2, 2, $\bar{4}$) As	8.85	7.70	(8.03, 0.83)	(7.26, 0.44)	(0.14, −0.15)	(0.55, −0.50)
P	7.77	6.84	(7.03, 0.58)	(6.44, 0.21)	(0.10, −0.09)	(0.31, −0.31)
Sb	7.32	6.47	(6.56, 0.47)	(6.05, 0.11)	(0.08, −0.06)	(0.22, −0.23)
N-(7, 7, $\bar{7}$) As	3.05	3.05	(3.26, −1.51)	(3.26, 1.51)	(0.17, −0.04)	(0.17, 0.04)
P	3.05	3.05	(3.15, −1.12)	(3.15, 1.12)	(0.11, −0.02)	(0.11, 0.11)
Sb	3.03	3.03	(3.07, −0.96)	(3.07, 0.96)	(0.08, −0.01)	(0.08, 0.01)
O-(4, 4, 4) As	6.08	6.08	(5.43, −0.17)	(5.43, −0.17)	(0.15, −0.29)	(0.15, −0.29)
P	5.60	5.60	(5.02, −0.17)	(5.02, −0.17)	(0.09, −0.17)	(0.09, −0.17)
Sb	5.38	5.38	(4.80, −0.10)	(4.80, −0.10)	(0.06, −0.13)	(0.06, −0.13)
P-(2, 2, 8) As	5.68	3.83	(4.69, 0.09)	(4.32, 0.50)	(0.12, −0.02)	(−0.07, 0.65)
P	5.31	3.69	(4.44, 0.00)	(4.01, 0.35)	(0.07, −0.01)	(−0.04, 0.39)
Sb	5.14	3.61	(4.29, −0.04)	(3.84, 0.29)	(0.04, −0.01)	(−0.03, 0.28)

TABLE II. *(Continued)*

Shell	EMT F_x	EMT F_z	I-M[b] F_x	I-M F_z	I-M G_x	I-M G_z
Q-(1,1,5) As	8.83	6.83	(8.66, 0.82)	(6.98, −0.89)	(−0.02, 0.12)	(−0.67, 0.02)
P	7.79	6.14	(7.21, 0.54)	(6.03, −0.64)	(−0.01, 0.07)	(−0.40, 0.01)
Sb	7.35	5.84	(6.56, 0.42)	(5.58, −0.53)	(0.00, 0.05)	(−0.29, 0.00)
R-(7,7,1) As	3.67	4.96	(3.27, 1.00)	(4.58, 1.81)	(−0.05, −0.03)	(−0.16, 0.02)
P	3.58	4.73	(3.24, 0.63)	(4.26, 1.28)	(−0.03, −0.02)	(−0.10, 0.02)
Sb	3.52	4.61	(3.20, 0.47)	(4.08, 1.05)	(−0.02, −0.01)	(−0.07, 0.01)
S-(2,2,$\overline{12}$) As	3.82	2.03	(2.86, −0.02)	(2.38, −0.46)	(−0.02, 0.07)	(−0.09, −0.18)
P	3.75	2.10	(2.90, 0.02)	(2.39, −0.34)	(−0.01, 0.04)	(−0.05, −0.11)
Sb	3.70	2.11	(2.89, 0.03)	(2.37, −0.30)	(−0.01, 0.03)	(−0.03, −0.08)
T-(2,2,12) As	3.82	2.03	(2.92, −0.26)	(2.36, 0.37)	(−0.02, 0.07)	(−0.09, 0.17)
P	3.75	2.10	(2.96, −0.20)	(2.37, 0.26)	(−0.01, 0.04)	(−0.05, 0.11)
Sb	3.70	2.11	(2.94, −0.18)	(2.36, 0.21)	(−0.01, 0.03)	(−0.03, 0.08)
U-(5,5,9) As	3.67	2.78	(3.11, 1.26)	(2.44, 0.90)	(−0.04, −0.03)	(0.01, −0.13)
P	3.61	2.79	(3.11, 0.93)	(2.52, 0.66)	(−0.02, −0.02)	(0.00, −0.08)
Sb	3.56	2.78	(3.08, 0.78)	(2.52, 0.55)	(−0.02, −0.01)	(0.00, −0.05)
X-(5,5,1) As	5.53	6.83	(4.37, −0.18)	(6.74, 3.08)	(−0.05, −0.19)	(0.04, 0.09)
P	5.14	6.24	(4.26, −0.11)	(5.86, 2.06)	(−0.03, −0.11)	(0.03, 0.05)
Sb	4.95	5.98	(4.18, −0.09)	(5.45, 1.63)	(−0.02, −0.08)	(0.02, 0.04)

[a] All values are in units of 10^{-3} Å$^{-3/2}$.

[b] This work.

numbers gives the a_l values calculated from Eq. (42), these a_l values are the main results of this work. Our new theoretical a_l values are closer to the experimental a_l values than are the EMT a_l values for all shells except shell E-(111) which will be discussed in Sec. III C6.

The calculation of the a_l values in the third column utilized no adjustable parameters for the purpose of improving agreement between theory and experiment. However, since the values of η and k_0 are not exactly known and since the use of the isotropic $F(r)$ from Eq. (27) is certainly an approximation, we have investigated the effects of changing η, k_0, $F(r)$, and ϵ_0 in the calculations. In order conveniently to examine the effects of these variations, we used a root-mean-square deviation[36]

$$\Delta = \left(N^{-1}\sum_l \left|(a_l^{(\text{theory})} - a_l^{(\text{exp})})/a_l^{(\text{exp})}\right|^2\right)^{1/2} . \qquad (47)$$

The sum over l was for all identified shells except the E-(111) shell for all three donors, so that $N = 63$. The location of these identified sites with respect to the donor site are illustrated in Fig. 6.

Table III summarizes the results obtained when $\epsilon_0 = 11.4$, $F(r)$ is given by Eq. (27), k_0 is varied using Eq. (46), and η is chosen to minimize Δ for each value of k_0 (LLSQ from the IBM Scientific Subroutine Package). The minimum value of Δ occurs for values of k_0 and η very close to the values $k_0/k_{\max} = 0.854$ and $\eta = 178$. Our minimum value of Δ is 11.2%, while the corresponding Δ for the EMT a_l values is 60.8%.

Calculations were also made with $\epsilon_0 = 11.7$. The a_l values based on Eq. (42) are much less sensitive to the value of the static dielectric constant than one might expect. This is probably due to the fact that the potential parameter U_0 in Eq. (6) is adjusted in each calculation so that the energy E in Eq. (19) agrees with the experimental ionization energy. We do not list any a_l values for $\epsilon_0 = 11.7$ since they varied only between 0.1% and 1% from the corresponding a_l values listed in Table I for $\epsilon_0 = 11.4$.

We also approximated $F(r)$ in Eq. (27) by various combinations of two exponentials. For example, the sixth column of numbers in Table I is based on $k_0/k_{\max} = 0.854$, $\epsilon_0 = 11.4$, $\eta = 178$, and $F(r)$ in Eqs. (16) and (22) is taken as

$$F(r) = 0.850(\pi 15^3)^{-1/2} e^{-r/15\,\text{Å}} + 0.211(\pi 5^3)^{-1/2} e^{-r/5\,\text{Å}} , \qquad (48)$$

which is shown as curve 2 in Fig. 2. The rms error Δ only increases to 13% for this choice of $F(r)$. When $F(r)$ is approximated by various combinations of two exponentials the minimum values of Δ always occur for combinations that are good approximations to the Whittaker-function-type solutions. In all of these investigations minimum values of Δ in the 11% to 13% range always oc-

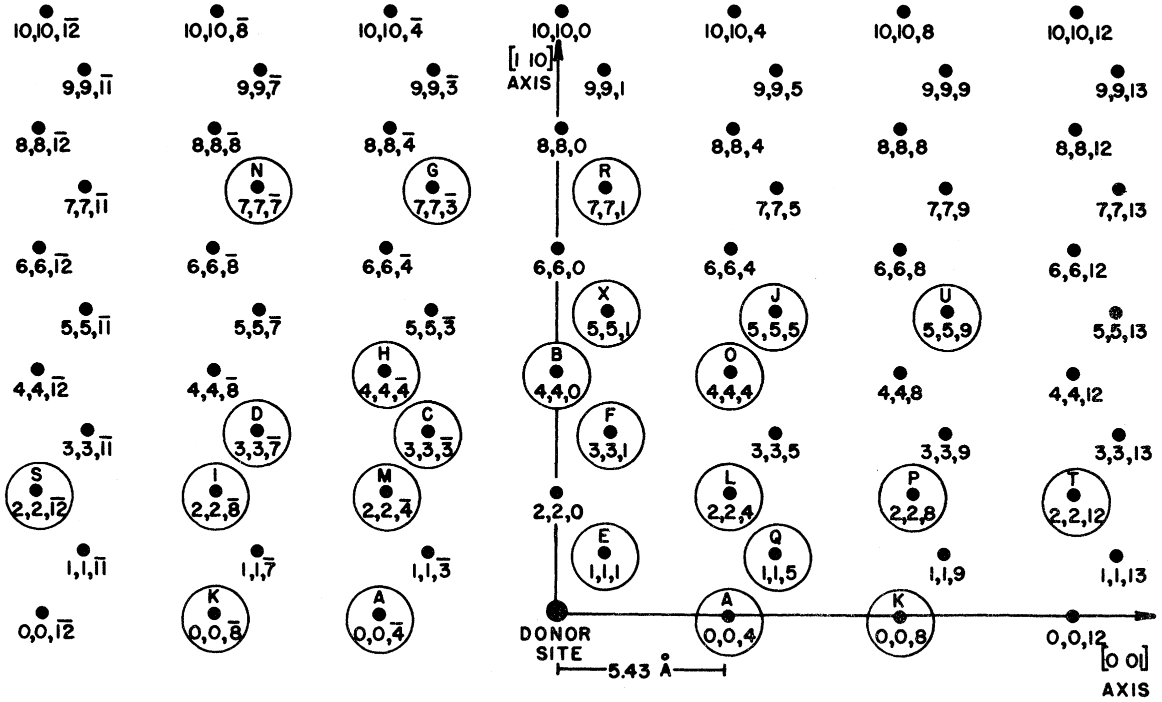

FIG. 6. Lattice sites that have been assigned to experimental ENDOR lines have the letter used to designate the experimental ENDOR line included within a circle about the site. A lattice site with the coordinates (n, n, $\bar{m}$) is equivalent by symmetry to the site with the coordinates (n, n, m).

curred for $k_0/k_{\max}$ within 0.005 units of 0.854 and values of η within 5% of the value 178.

Therefore we see that without the use of any parameters specifically to "fit" the hyperfine constants, the procedure described in Sec. II gives a_l predictions with a factor-of-5 improvement over the EMT a_l predictions. Furthermore, when we investigate the effects of slight changes in those quantities for which there is some uncertainty or approximation involved, our results are insensitive to slight changes in ϵ_0 and the shape of $F(r)$ and the best agreement with experiment occurs for the accepted values of 178 for η and for the values of 0.854 for $k_0/k_{\max}$ that comes out of the pseudopotential program that calculates the Bloch functions.

A convenient presentation of the trends of the dependence of the Fermi-contact values of the different lattice sites on the donor ionization energy in the range of 42–54 meV is given in Figs. 7–10. The solid lines correspond to the third column of a_l values in Table I, and the dashed lines correspond to the EMT a_l values in the second column. The dependence of the contact values on k_0 is shown in Figs. 11 and 12 for the phosphorus donor. These figures are similar to Figs. 5–7 of Ref. 5 and Fig. 8 of Ref. 3, except that we have used Eq. (46) instead of the EMT Eq. (43). As we said before, the uncertainty in k_0 necessitated an examination of the dependence of a_l on k_0, but no improvement in agreement between theory and experiment was obtained from these considerations. This can also be seen in Figs. 11 and 12, where the experimental points are rather randomly scattered about the value of $k_0/k_{\max} = 0.854$.

B. Discussion of the piezohyperfine constants

The results of the study by Hale and Castner[6] of the changes in the a_l values when uniaxial stress

TABLE III. rms deviation of calculated values from experimental values for "best-fit" value of η.

$k_0/k_{\max}$	η	Δ (%)
0.80	157.20	40.94
0.81	161.60	35.27
0.82	166.03	29.18
0.83	170.31	22.82
0.84	174.16	16.61
0.85	177.23	11.95
0.85417	178.18	11.24
0.86	179.08	12.08
0.87	179.24	17.49
0.88	177.29	25.12
0.89	173.02	33.39
0.90	166.51	41.56

was applied are listed in column 7 of Table I. The numbers tabulated are the i.d. parameters defined by Hale and Castner and are a measure of the linear perturbation effects of the applied stress. For reasons of space the reader is referred to Ref. 6 for the definition of the experimental i.d. parameter and the derivation of its theoretical expression based on the EMT. There are two columns of theoretical i.d. parameters listed in Table I. Column 8 is based on Eq. (23) of Ref. 6. Column 9 of Table I is based on our "interpolation envelope functions" F^C; in this case, the term $F_j^R(\vec{R}_l)\cos(\vec{k}_{0j}\cdot\vec{R}_l)$ in Eq. (23) of Ref. 6 is replaced by

$$[F_j^R(\vec{R}_l)\cos(\vec{k}_{0j}\cdot\vec{R}_l) - F_j^I(\vec{R}_l)\sin(\vec{k}_{0j}\cdot\vec{R}_l) + G_j^R(\vec{R}_l)] \; .$$

Examination of the last three columns of Table I for the previously identified shells A-(0, 0, 4) and B-(4, 4, 0) indicates that a criterion of "good agreement" would seem to be that the experimental and theoretical i.d. parameters have the same sign and agree within a factor of 2 in magnitude (unless they

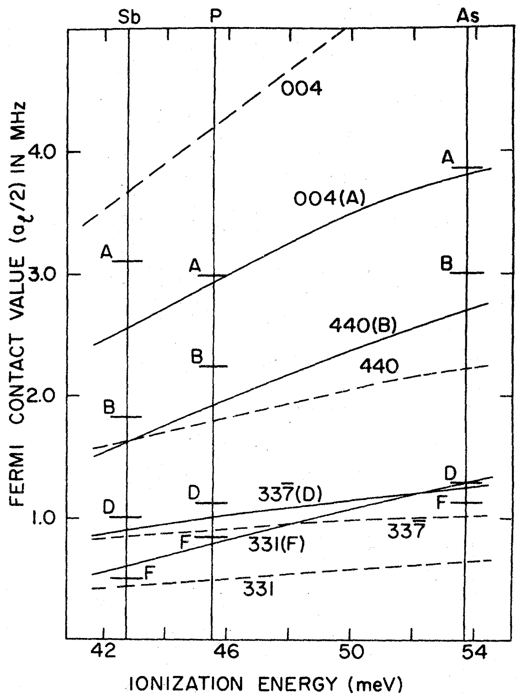

FIG. 7. Fermi-contact values for shells A-(0, 0, 4), B-(4, 4, 0), D-(3, 3, $\bar{7}$)E-(1, 1, 1), and F-(3, 3, 1) as a function of ionization energy. The vertical lines indicate the experimental ionization energies of the three shallow donors As, P, and Sb. The short horizontal lines marked on the vertical lines indicate the experimental a_l values for the various ENDOR lines for the three donors. The solid curves give the calculated values obtained from Eq. (42). The dashed lines are the predictions of a_l from EMT.

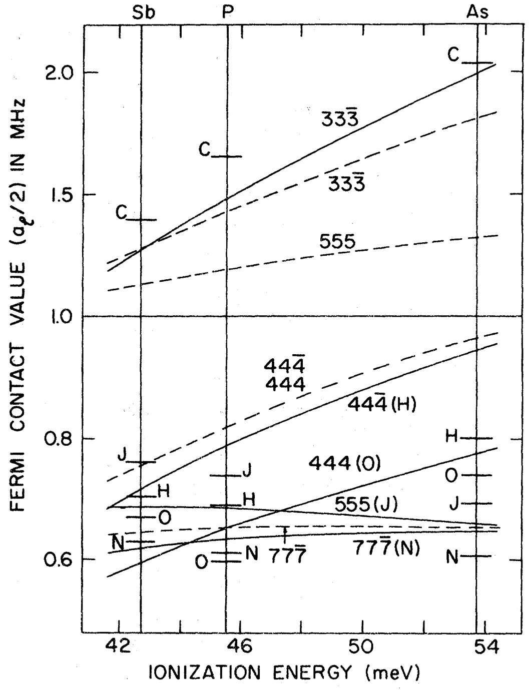

FIG. 8. Fermi-contact values a_l as a function of ionization energy for shells along ⟨111⟩ axes. The format is the same as in Fig. 7.

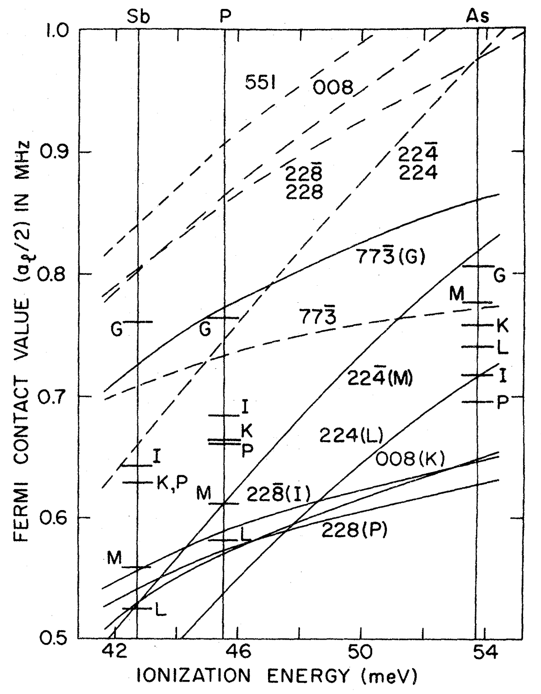

FIG. 9. Fermi-contact values a_l as a function of ionization energy. The format is the same as in Fig. 7.

are very small in magnitude). Examination of the i.d. values for the rest of the shells shows good agreement, which provides additional independent support for the assignments between experimental shells and lattice sites that we have made on the basis of our new theoretical a_l values. Now that the shells have been identified it is possible to see that the accuracy of i.d. values based on the EMT is about the same as the accuracy of the a_l values based on the EMT.

We have used the "interpolation envelope function" to calculate the i.d. parameter for the phosphorus donor as a function of k_0 as shown in Fig. 13. Figure 13 also helps to illustrate the additional support provided by the strain data for our assignments of lattice sites to ENDOR lines. For example, as one examines Figs. 6–11 if there seems to be some doubt about distinguishing between two shells of the same symmetry and similar a_l values, then examination of Fig. 13 usually shows very different i.d. values for the shells in question.

The i.d. parameters based on the "interpolation envelope function" differ somewhat from the EMT i.d. values, but the over-all average agreement with experiment is about the same for both sets of numbers. This is because our new i.d. numbers are not obtained in the same way that our new a_l values are obtained. To calculate a_l values

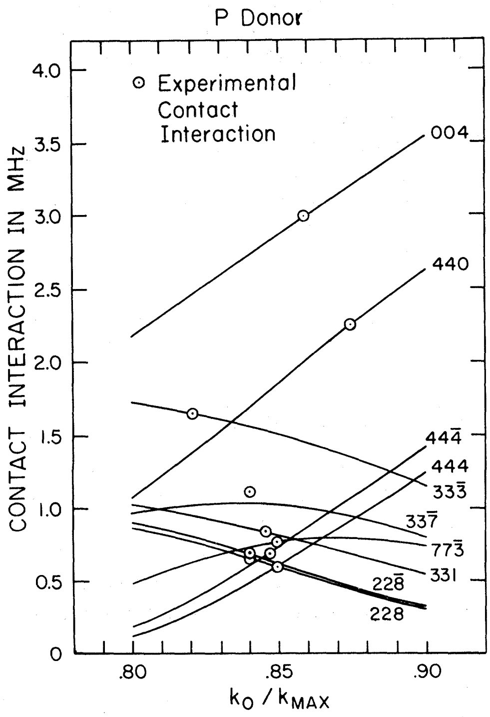

FIG. 11. Fermi-contact values a_l, as a function of k_0 as given by Eq. (46).

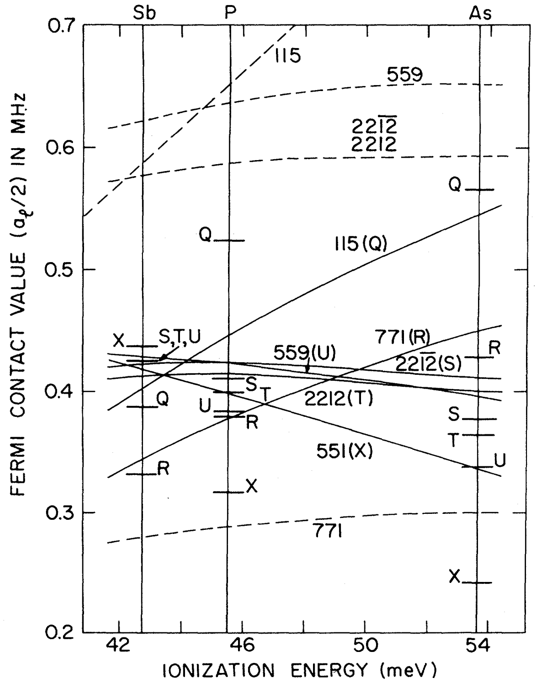

FIG. 10. Fermi-contact values a_l as a function of ionization energy. The format is the same as in Fig. 7.

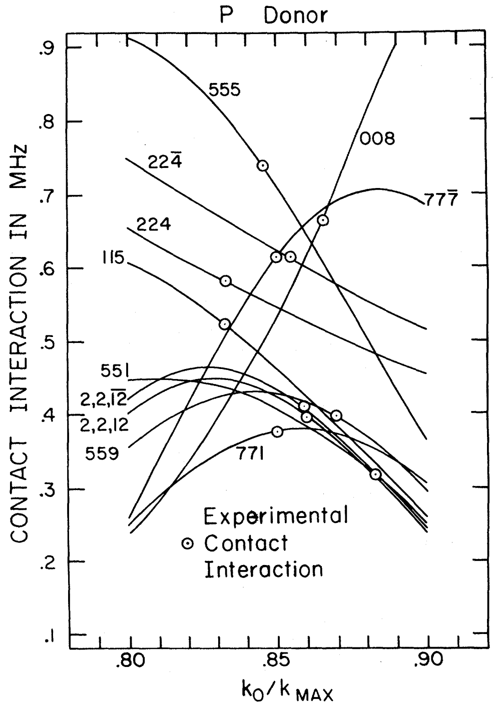

FIG. 12. Fermi-contact values a_l as a function of k_0 as given by Eq. (46).

for a strained lattice properly one should start with the EMT wave function[6] and the Bloch functions for the strained lattice and calculate a new set of $A_n(\vec{k})$. Because the strained lattice has a lower symmetry there would be more nonequivalent points in k space to consider. Such a calculation would probably take at least an order of magnitude more computer time than our calculation of a_l values and we have not attempted it.

C. Discussion of individual shells

Since the correlation of experimental ENDOR lines with Si lattice sites was previously known[3,5,6] for only five of the 22 shells listed in Table I, we discuss in this section our reasons for our identifications and some of the characteristics of the various shells.

1. Shells A, B, K, and Q

The identifications A-(0, 0, 4), B-(4, 4, 0), Q-(1, 1, 5), and K-(0, 0, 8) were already known[3-6] and, therefore, were the first shells that we examined for improved agreement between the theoretical and experimental a_l values. All the theoretical a_l values for these shells in column 3 of Table I represent improvements over the results of EMT in column 2.

2. Shells D, F, and G

The shells D, F, and G all have the symmetry of a general site in a $\{110\}$ plane. The theoretical a_l values from column 3 of Table I are close to the experimental values for the assignments D-$(3, 3, \bar{7})$, F-(3, 3, 1), and G-$(7, 7, \bar{3})$. Also, the theoretical and experimental i.d. strain parameters listed in columns 7–9 in Table I agree well for these assignments. As discussed in Ref. 4, it was suspected that the ENDOR shell labeled as the V shell in antimony might be the "missing" F shell for this donor. On the basis of the present work we are even more convinced of this and, therefore, have listed the V(Sb) shell along with the F(As) and F(P) shells.

3. Shells I, P, L, and M

A set of lattice sites with the site coordinates (n, n, m) and $(n, n, \bar{m})$ are related by inversion. Such inversion-related shells occur when n and m are nonzero even numbers such as (2, 2, 4) and $(2, 2, \bar{4})$. The theoretical a_l values predicted by EMT are equal for the inversion-related shells although this is not required by the symmetry of the donor problem. One of the new features of the present work is that we predict different a_l values for the inversion-related shells.

The assignment I-$(2, 2, \bar{8})$; P-(2, 2, 8), L-(2, 2, 4), and M-$(2, 2, \bar{4})$ are supported by the values of a_l, the magnitudes of the inversion splittings, the general trend as a function of donor ionization energy (see Fig. 9) including the fact that M and L are below I and P for antimony but above I and P in arsenic. Again the theoretical and experimental i.d. strain parameters are in agreement for these assignments.

4. Shells C, J, H, O, and N

The experimental angular dependencies of the ENDOR lines for shells C, J, H, O, and N have the symmetry of sites along the $\langle 111 \rangle$ directions. It is not possible to decide on the basis of the EMT a_l values whether the sites $(3, 3, \bar{3})$ or (5, 5, 5) should be identified with shell C. Examination of Fig. 8 shows that site $(3, 3, \bar{3})$ corresponds to shell C and that site (5, 5, 5) is no longer a possible assignment. Note especially that the theoretical and experimental a_l values for shell J-(5, 5, 5) decrease with increasing ionization energy. Most shells have experimental a_l values that increase with increasing ionization energy, but the a_l values for shells J, N, S, T, U, and X decrease with increasing donor energy. Our theoretical results for these shells have this dependence except for shell N-$(7, 7, \bar{7})$ which has the smallest experiment-

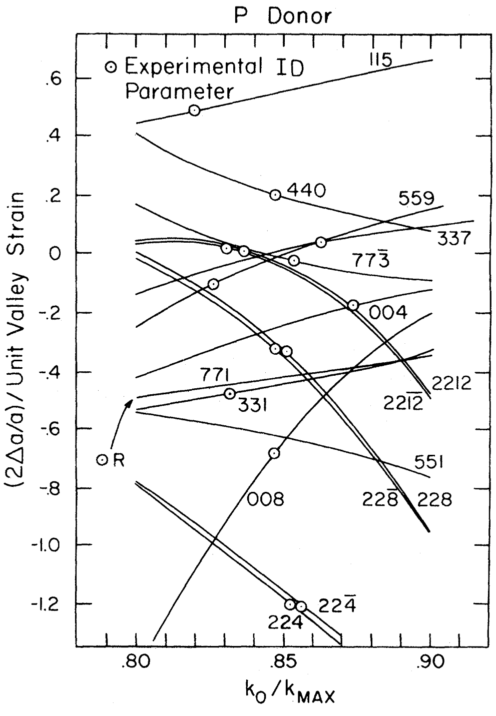

FIG. 13. Theoretical i.d. strain parameters as a function of k_0.

al decrease of any of the shells. In fact, our results for the two exponential approximation for $F(r)$ (column 6 of Table I) do show a slight decrease for the shell-N a_l values.

The shells C, J, and N are characterized (see Table II of Ref. 4) by very small anisotropic hyperfine interactions B_{xy} but the shells H and O have B_{xy} values an order of magnitude larger than the values for shells C, J, and N and would appear to "belong" together. The $(4, 4, \overline{4})$ and $(4, 4, 4)$ inversion-related sites are the only possible assignments for shells H and O in the present theory. The experimental a_l values for the H and O shells of phosphorous have an anomalous behavior (as does shell A also) in that they are smaller than either the antimony or arsenic a_l values. Also, the experimentally observed inversion splitting varies more from donor to donor for the H and O shells than for the I, P, L, and M shells. Nevertheless, we are confident of the assignments H-$(4, 4, \overline{4})$ and O-$(4, 4, 4)$.

There are no first-order strain effects for sites along the $\langle 111\rangle$ axes so there are no linear i.d. parameters to consider.

5. Shells R, S, T, U, and X

The shells R, S, T, U, and X all have the symmetry of general sites in the $\{110\}$ planes. The assignment R-$(7, 7, 1)$ is supported by the magnitude of the a_l values and by the i.d. strain parameters. The assignments S-$(2, 2, \overline{12})$ and T-$(2, 2, 12)$ provide good agreement for the a_l values, the inversion splitting, and the decrease in a_l for increasing donor ionization energy. This is the fourth inversion-related shell pair to be identified in this work. For all four pairs the $(n,n,\overline{m})$ site has a larger Fermi-contact interaction and larger anisotropic hyperfine interactions. The S-$(2, 2, \overline{12})$ and T-$(2, 2, 12)$ assignments are also in fair agreement with the i.d. parameters measured for the phosphorous donor. This should be taken with some reservation, however, because in the experimental data for phosphorous there is a cluster of ENDOR lines due to the S, T, U, and R shells. This fact makes it difficult to analyze the stress-induced changes, especially for the S and T lines which also have very small anisotropic splittings (small values of B_{ij}).

The assignment U-$(5, 5, 9)$ is made on the basis of the magnitude of the a_l values and the energy dependence of the a_l values. The strain i.d. parameter for $U(P)$ seems to agree for this assignment but, for the same reasons discussed above for the S and T shells, the experimental i.d. value may not be reliable for the $U(P)$ shell.

It was reported in the original strain investigation[6] that the i.d. parameter for shell X was less than zero, but its value could not be determined. Since our a_l calculations suggest the assignment X-$(5, 5, 1)$ and since the theoretical i.d. value for site $(5, 5, 1)$ is in the range from -0.3 to -0.8, we reexamined the experimental strain data that was kindly supplied to us by Hale and Castner. As a result we believe that the i.d. parameters for X(Sb) and for X(P) are about -0.4 to -0.6 [the data were not available for X(As)]. These values are certainly within our agreement criterion discussed in Sec. III B. Both the theoretical and experimental a_l values for shell X decreases more rapidly with increasing ionization energy than for any other shell with this feature and are drastically different from the EMT predictions.

6. E shell

The E shell has always been identified[3-5] as the $(1, 1, 1)$ site because it has a very large anisotropic hyperfine interaction. This is the only shell for which our theoretical a_l values are not in good agreement with experiment. We do not believe that this is due entirely to any numerical feature of our calculation (such as too coarse a grid in reciprocal-lattice space) that is producing a large error for sites near the donor. One reason for this belief is the fact that our calculated contact interactions for donor nuclei (see Sec. III D) are 50% to 70% of the experimental values, whereas the values for the E shell are factors of between 6 and 200 too small. The $(1, 1, 1)$ site is the nearest-neighbor site for the donor, yet there are many sites with larger contact interactions. From the point of view of the EMT approximations, the small value of a_l for $(1, 1, 1)$ is due to its location very near a node of the standing wave pattern formed by the six conduction-band minima (see Fig. 15). For a single-valley EMT wave function the theoretical a_l for $(1, 1, 1)$ would be about 20 times larger than it is for all six valleys. Therefore, an order-of-magnitude cancellation is involved in the determination of a_l for $(1, 1, 1)$. The real part of the interpolation envelope functions F^C listed in Table I for the E-$(1, 1, 1)$ shell are about one half as large as the EMT envelope functions for this shell. However, the theoretical a_l values are not just a factor of 4 smaller than the EMT a_l values but instead are smaller by factors of 6 to 200. These very small a_l values for the $(1, 1, 1)$ shell in our results are due to an additional cancellation between the contributions of the real and imaginary parts of F^C. Although F_j^I is always smaller than F_j^R (see Table I), whenever $\cos(\vec{k}_0 \cdot \vec{R}_l)$ is near zero and $\sin(\vec{k}_0 \cdot \vec{R}_l)$ is near unity, then F_j^I is very important. This can also be seen in column 5 of Table II, for which F^I in Eq. (46) has been set equal to zero. Therefore, we believe that our poor prediction for the E-(1, 1, 1) shell is due to some feature such as lattice relaxation that affects this site more than it does the more distant sites and that the apparently better predictions of the EMT for this one shell is just a numerical accident.

7. "Missing" shells in antimony

For the antimony donor the F, J, K, N, T, and U shells were not located in the original work,[4] and the present work indicates that the S and L shells were improperly located. On the basis of the present work, the study of line intensities in the original experimental data, the stress work by Hale and Castner,[6] and private communications with Hale, the locations of these shells are deduced to be as follows. Line J(Sb) is thought to be behind the G(Sb) line that has a small anisotropy and such a small strain parameter that it does not shift appreciably under stress to expose the J(Sb) shell.[37] Line N(Sb) is believed to be the $\langle 1, 1, 1\rangle$-axis symmetry shell which Hale and Castner[6] located behind the P(Sb) line at $a_l/2 = 629$ kHz by stress measurements. It is also probable that line K(Sb) is in either the same cluster or in the cluster formed by lines M(Sb), L(Sb), and V(Sb) at approximately $\frac{1}{2}a_l = 525$ kHz. At this time the most probable location is thought to be in the I, P, N cluster. The V(Sb) line has been taken to be the "missing" F line. The cluster at $\frac{1}{2}a_l = 425$ kHz, where line L(Sb) was originally thought to lie, is now taken to be composed of the S, T, and U lines. The experimental values based on these assignments are listed in the experimental column of Table I and, also, are used in Figs. 7–12.

8. Shells and lattice sites not identified

The experimental ENDOR spectra show a large number of Si^{29} ENDOR lines (see Fig. 2 of Ref. 4) with values of $\frac{1}{2}a_l$ less than 300 kHz. The experimental ENDOR signal-to-noise ratio in this region is excellent (1000 to 1 and better), and for any given crystal orientation there are many resolved lines (by the Rayleigh criterion). Nevertheless, no successful analysis has been made of the data in this region because the large number of lines pass back and forth through one another making it difficult to follow the angular dependence of the lines. Perhaps this region can some day be analyzed by a combined theoretical and experimental effort in which case possibly as many as an additional 20 shells could be tabulated. However, since the linewidth is about 3 kHz and many of the lines with $\frac{1}{2}a_l < 300$ kHz are actually sites near the donor with large cancellation effects such as discussed above for shell E-(1, 1, 1), it will require a theory with at least 1% and possibly 0.1% overall accuracy to assist much in the interpretation of this region. For completeness we list in Table IV the theoretical predictions of several shells with a_l values smaller than the identified shells listed in Table I. The shells in Table IV have not been correlated with any experimental data.

D. Fermi contact interaction for donor nuclei

The Fermi-contact interaction values that measure the density of the donor electron at the nucleus of the donor (As, P, Sb) have been determined previously by ESR and ENDOR.[3] The experimental values are given in column 1 of Table V for P^{31}, As^{75}, Sb^{121}, and Sb^{123}. Also given in **columns 4 and 5 in Table V are the theoretical** values that have been calculated from Eq. (42), with two modifications. First, the factor g_n of the particular donor nucleus must be used. Second, the pseudopotential Bloch function must now be orthogonalized to a donor core instead of a silicon core. Consequently, we have multiplied the value

TABLE IV. Theoretical values of $a_l/2$ and i.d. for some shells not yet identified.

Shell	EMT $\frac{1}{2}a$	I-M[a] $\frac{1}{2}a$	EMT i.d.	I-M i.d.
(2, 2, 0) As	608	394	−2.840	−3.128
P	431	304	−2.799	−2.913
Sb	367	266	−2.784	−2.804
(1, 3, 7) As	360	351	3.790	1.013
P	319	310	3.577	1.250
Sb	300	288	3.506	1.366
(0, 4, 8) As	455	339	−0.640	−0.690
P	401	299	−0.645	−0.677
Sb	376	278	−0.647	−0.671
(10, 10, 0) As	285	279	0.313	0.421
P	295	272	0.300	0.361
Sb	296	264	0.295	0.335
(9, 9, 5) As	368	258	0.098	0.068
P	382	284	0.091	0.053
Sb	383	289	0.088	0.047
(1, 5, 9) As	433	252	0.329	1.040
P	413	266	0.342	0.848
Sb	400	266	0.347	0.779
$(3, 3, \overline{11})$ As	309	309	−0.181	−0.276
P	302	291	−0.170	−0.217
Sb	295	278	−0.166	−0.190
$(7, 7, \overline{11})$ As	278	262	−0.229	−0.221
P	296	275	−0.224	−0.216
Sb	299	275	−0.222	−0.214

[a] This work.

of $|u_0^0(k_0, \vec{R}_l)|^2 = \eta = 178$ for silicon by a ratio of calculated silicon and donor wave functions $\eta_D/\eta_{\text{Si}} = |\psi_{ns}(0, D^+)|^2/|\psi_{3s}(0, \text{Si}^0)|^2$. $\psi_{ns}(0, D^+)$ indicates the value of ψ at the donor nucleus, $r = 0$, for a valence s electron for a singly ionized donor, $\psi_{3s}(0, \text{Si}^0)$ indicates the value of ψ at the silicon nucleus, $r = 0$, for a valence s electron bound to a neutral silicon atom, Si^0. The wave-function densities are obtained from a Hartree-Fock-Slater self-consistent atomic-field computer program[32] originally written by Herman and Skillman. Also listed in column 4 of Table V for comparison are the EMT a_l values obtained by using $F(0)$ from Eq. (27).

The theoretical values in column 5 of Table V are 50% to 70% of the experimental values. There are at least two reasons for the fact that our theoretical values are too small. The first is that when the shallow-donor "conduction-band" electron is near a given lattice site it really moves in the (approximate) potential of a neutral silicon or an ionized donor so that a comparison of wave functions for Si^- and D^0 might be more nearly the physical equivalent of our problem. Therefore, the ratio of electron density at the donor nucleus to that at the silicon nucleus is probably larger than the ratio we have used. The second reason is that our calculation of $A_n(\vec{k})$ was limited to the first four conduction bands. Either a cutoff at insufficiently large $\vec{k}$ values or $A_n(\vec{k})$ values too small for $\vec{k}$ distant from k_0 would have the largest effects for small values of r. Therefore, we do not consider it surprising that the theoretical values in Table V are somewhat too small.

To test this hypothesis we evaluated the separate contributions to the wave-function density at the donor sites from each of the eight bands used in this study. Given in Table VI are the individual contributions to $F_x(0)$ and $G_x(0)$ as defined in Eqs. (44) and (45). One can see from columns 7 and 8 that there is an appreciable contribution $[G(0)]$ from the other bands. For the other lattice sites listed in Table I the contributions from the other bands (the G term) are small. However, the contributions of the other bands to the donor site are larger because the $e^{i\vec{k}\cdot\vec{r}}$ term is unity and does not oscillate as we sum over $\vec{k}$. Since the valence and conduction bands give contributions of opposite sign, it would be expected that additional conduction bands would decrease the magnitude of $G(0)$. In fact, if one ignores the contributions of the other bands the values listed in the last column of Table V are much closer to the experimental values. Nevertheless, one should not conclude that the contributions of the other bands are not significant for all the hyperfine interactions, since we discuss in Sec. IV the reasons for believing that contributions of the other bands are probably significant even for a calculation of this accuracy. Our conclusions from this study are that one must consider more conduction bands in future work for increased accuracy of the donor hyperfine interactions and must make a more accurate consideration of the orthogonalization of the donor electron to the donor ion.

TABLE V. Calculated and experimental values[a] of donor ESR hyperfine constants.

Donor	Expt[b] $\frac{1}{2}a_l$	$\frac{g_D}{g_{\text{Si}}}$	$\frac{\eta_D}{\eta_{\text{Si}}}$	EMT $\frac{1}{2}a_l$	$\frac{1}{2}a_l$[c] $F_x + G_x$	$\frac{1}{2}a_l$[c] F_x
P^{31}	58.76	2.0377	1.4522	224	35.6	56.0
As^{75}	99.17	0.8621	3.3831	425	60.0	105
Sb^{121}	93.40	1.2048	4.1193	274	44.7	65.8
Sb^{123}	50.76	0.6524	4.1193	149	24.2	35.6

[a] All values of $\frac{1}{2}a_l$ are in MHz.

[b] Experimental data from Ref. 3.

[c] Calculated as discussed in Sec. IIID of this paper from the F_x and G_x given in Table VI.

IV. COMPARISON OF THIS WORK WITH EFFECTIVE-MASS THEORY

The discussion of Sec. III shows that the theoretical predictions of the present calculation are in much better agreement with the experimental Si^{29} contact interactions than is the case for calculations based on the effective-mass theory. Therefore, an effort has been made to examine some details in order to have a better understanding of the similarities and differences of these two approximate representations of the shallow-donor ground-state wave function.

Since the EMT has been used in the previous attempts to interpret the experimental ENDOR results, and an effective-mass-type wave function [see Eqs. (13), (14), and (27)] is the starting point of this work, we present in Figs. 14 and 15 some idea of the wave functions involved. Figure 14 is a contour plot in the $\{110\}$ planes of the square, real part, and imaginary part of the cellular part, $u_n(\vec{k}, \vec{r})$, of the pseudopotential Bloch function for the conduction-band minima for which one hundred plane waves were used in the calculation. In Figs. 14(a)–14(c) show the band minimum k_0 vector at 45° to the plane and Figs. 14(d)–14(f) are for k_0 at 45° in the plane of Figs. 14 along the horizontal axis. For reasons of space we show the minimum area necessary to generate the entire $\{110\}$ planes. In fact we show only one half of the $\{110\}$ planes within the primitive cell; the rest of the plots within the cell may be obtained by reflection through the top of the plot. The

TABLE VI. Contributions to donor "envelope functions" from individual bands.

Donor	Band No. 1	No. 2	No. 3	No. 4	No. 5	No. 6	No. 7	No. 8	F_x [a]	G_x [b]
As	−3.19	−3.93	−0.95	−0.25	18.63	3.97	1.50	1.32	22.60	−5.49
P	−1.91	−2.36	−0.59	−0.15	13.83	2.58	0.90	0.78	16.40	−3.32
Sb	−1.36	−1.70	−0.44	−0.11	11.75	1.99	0.65	0.55	13.74	−2.41

[a] F_x is the sum of the contributions from band Nos. 5 and 6 according to Eq. (44).

[b] G_x is the sum of the contributions from band Nos. 1–4 and from band Nos. 7 and 8 according to Eq. (45).

circles around the lattice sites have radii of 0.38 Å which correspond to the positions of the outermost nodes of the 3*s* and 3*p* electrons of silicon. It is, of course, not feasible to show the corresponding plots for all of the 200 independent Bloch functions used in this calculation. Nevertheless, inspection of Fig. 14 makes it clear that it is not suprising that the calculated $A_n(\vec{k})$ values from Eq. (15) are in general complex numbers.

Figure 15 is a plot of the electron density of the linear combination of the six conduction-band minima Bloch functions. This is $|\Psi_c(\vec{r})|^2$ for the $\Psi_c(\vec{r})$ defined in Eq. (14). If this plot is multiplied by $F^2(r)$ as given in Eq. (27), it is then the starting EMT wave function used in this calculation. However, since $F(r)$ falls off slowly over a lattice distance (the assumption on which EMT is based), the shape of the contours are more or less un-

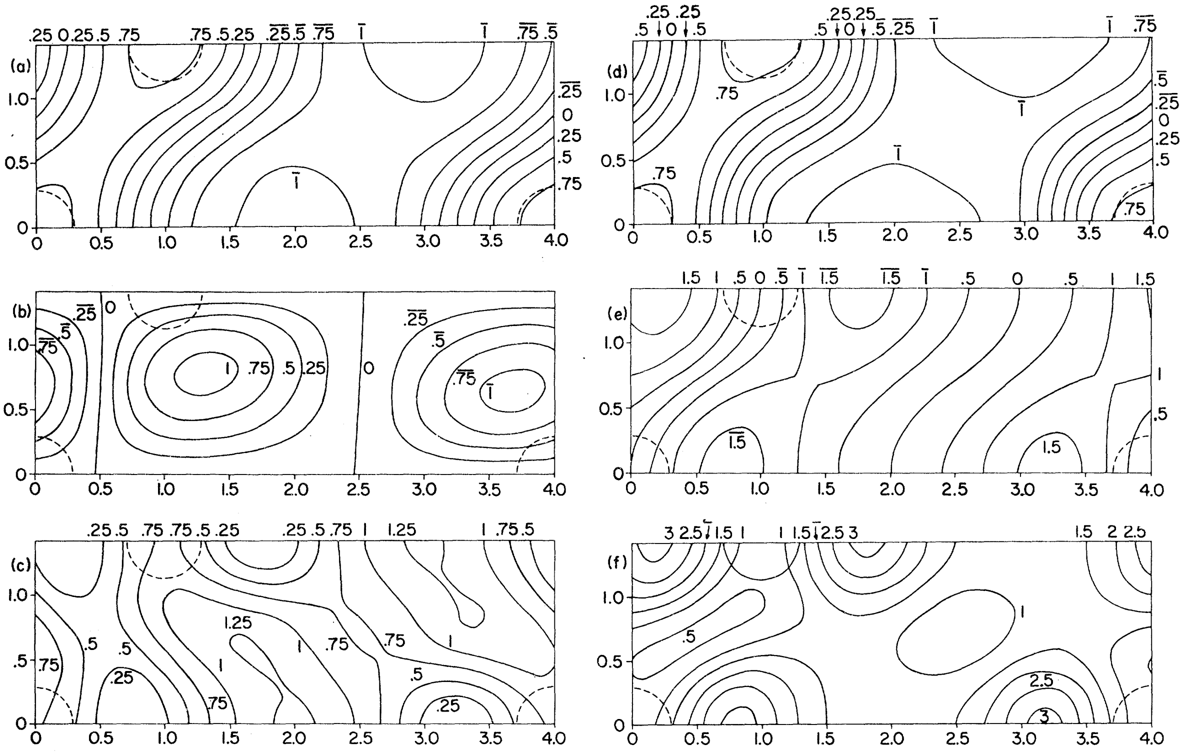

FIG. 14. Contour plots in the $(1\bar{1}0)$ plane based on the one hundred plane-wave expansion of $u_5(\vec{k}_0, \vec{r})$, the cellular part of the conduction-band minimum Bloch function. The horizontal direction is [001] and the vertical direction is [110]. The horizontal and vertical axes are labeled in silicon units such that (1,1,1) is a nearest-neighbor position. The dashed circles centered on (0,0,0), (1,1,1), and (0,0,4) have radii of 0.38 Å, which corresponds to the outermost node of 3*s* and 3*p* electrons for atomic silicon. (a) Plot of the real part of $u_5(\vec{k}_{0x}, \vec{r})$ when $\vec{k}_0$ is in the [100] direction making a 45° angle with the plane of the contour plot. (b) Plot of the imaginary part of $u_5(\vec{k}_{0x}, \vec{r})$ for $\vec{k}_0$ in the [100] direction. (c) Plot of $|u_5(\vec{k}_{0x}, \vec{r})|^2$. (d) Plot of the real part of $u_5(\vec{k}_{0z}, \vec{r})$ when $\vec{k}$ is in the [001] direction along the horizontal axis or [001] direction. (e) Plot of the imaginary part of $u_5(\vec{k}_{0z}, \vec{r})$. (f) Plot of $|u_5(\vec{k}_{0z}, \vec{r})|^2$.

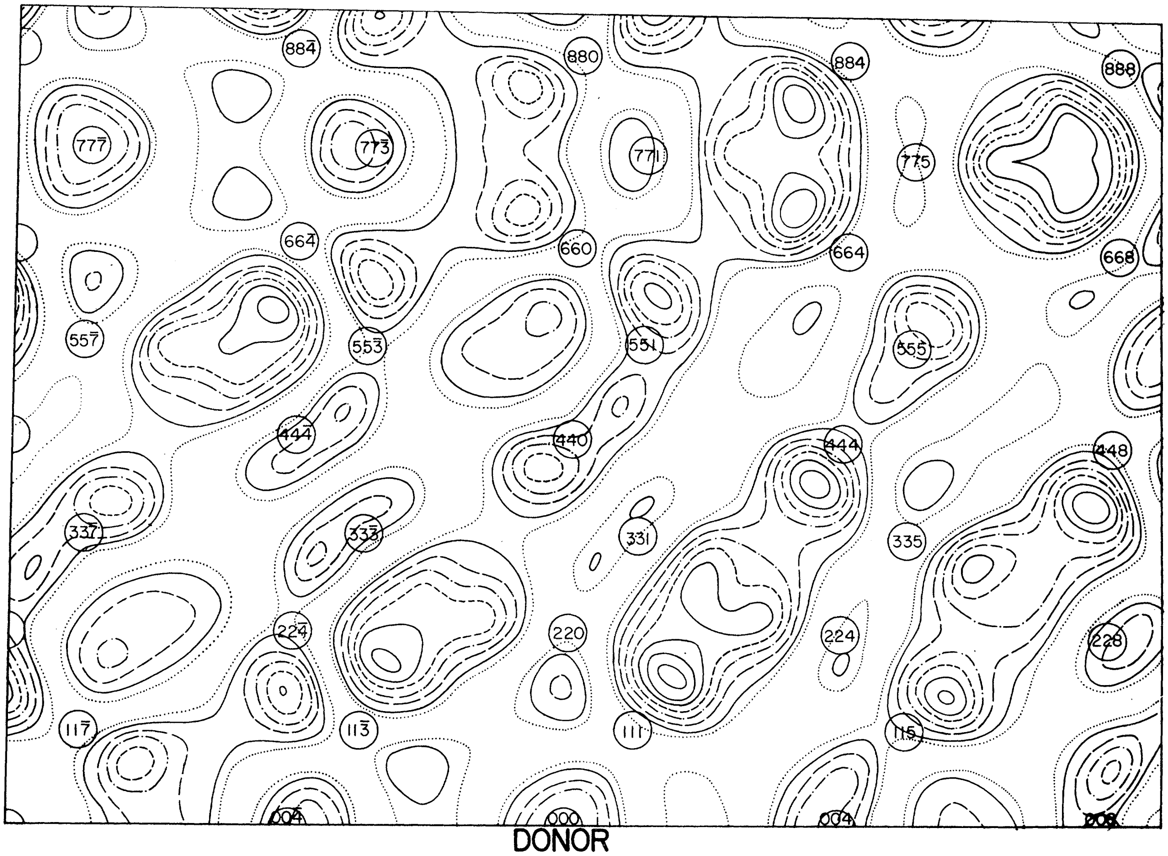

ATOM COORDINATES ARE GIVEN IN SILICON UNITS (SILICON UNIT = 2.57 a.u.)

FIG. 15. Plot of the electron density of $|\Psi_c(\vec{r})|^2$ for $\Psi_c(\vec{r})$ in Eq. (14). Dotted lines correspond to the value 0.5; solid lines to 1.0; long broken lines to 2.0; dashed-dotted lines to 3.0; short broken lines to 4.0; solid lines inside the short broken lines to 5.0, 6.0, and 7.0, respectively.

changed when multiplied by the envelope function. For comparison a similar plot made without including the details of the cellular part of the Bloch function may be seen in Fig. 2 of Ref. 5. Since a plot like Fig. 15 requires a determination of $|\Psi|^2$ at many points and not just at the lattice sites, it was not feasible for us to make such a plot of our new wave function. However, since the predictions of the EMT agree within a factor of 2 with experiment for most lattice sites, the general appearance of the contours of such a plot for our wave-function density should be similar to Fig. 15. Also, one can observe in Fig. 15 that lattice sites [e.g., $(1,1,\bar{3})$, $(1,1,\bar{7})$, $(2,2,0)$, $(3,3,5)$] near the donor that have not yet been experimentally identified because of small a_l values are at positions of very small values of Ψ_c and some of the more distant sites that have been identified [e.g., $(7,7,\bar{7})$, $(7,7,\bar{3})$, $(7,7,1)$, $(2,2,8)$] are at or near maxima of the Ψ_c standing-wave pattern.

Although $A_n(\vec{k})$ was calculated for four valence and four conduction bands, all bands other than the two lowest conduction bands were found to make a negligible contribution to the ionization energy and a small contribution to the Fermi-contact interactions. This point is illustrated by the fourth column of numbers of Table I for which the calculation was made using only the two lowest conduction bands, i.e., we let $G^R = 0$ in Eq. (46). The numbers in this column differ very little from other columns calculated using all eight bands. Since the rms error for the fourth column increases to only 12.5%, it is not clear that the contributions of the other six bands are significant in this work. On the other hand, if one examines the five shells (D, L, M, N, Q) for which the numbers change by 10% or more when G is set equal to zero, then the rms error for just these 15 numbers increases from 7.3% $(G \neq 0)$ to 12.8% $(G = 0)$. This is an indication that the contribution of the other six bands is significant to the calculations reported here and to any future attempts to improve on the present results.

The small effects of the other bands are due to the energy factor $[E(\vec{k})-E]$, to the matrix elements $(n\vec{k}|U_p^s(r)F(r)|n_0\vec{k}_{0j})$, and to the Bloch function values $u_n(k, \vec{R}_l)$. Those bands that are close in energy to the lowest conduction bands generally have small matrix elements as well as small values of $u_n(\vec{k}, \vec{R}_l)$ for $\vec{k}$ near $\vec{k}_0$ (because of their different symmetries and atomic character). The lowest two valence bands have relatively larger values of the matrix elements and Bloch functions but also larger values of the energy factor.

Figure 16 shows plots of $A_n(\vec{k})$ for phosphorous along the Δ axis for the two lowest conduction bands. The solid line represents the $A_n(\vec{k})$ values calculated in this work. The dashed line labeled 1 is the Fourier transform of the spherical Whittaker-type function $F(r)$ given by Eq. (27) that is used as the envelope function for the starting EMT wave function; this is the same as line 1 in Fig. 3. The dashed line labeled 4 is the Fourier transform of the EMT anisotropic envelope function and is the same as line 4 in Fig. 3. The lowest lines in the region of $k/k_{\max}$ between 0.6 and 1.0 are for the second conduction band.

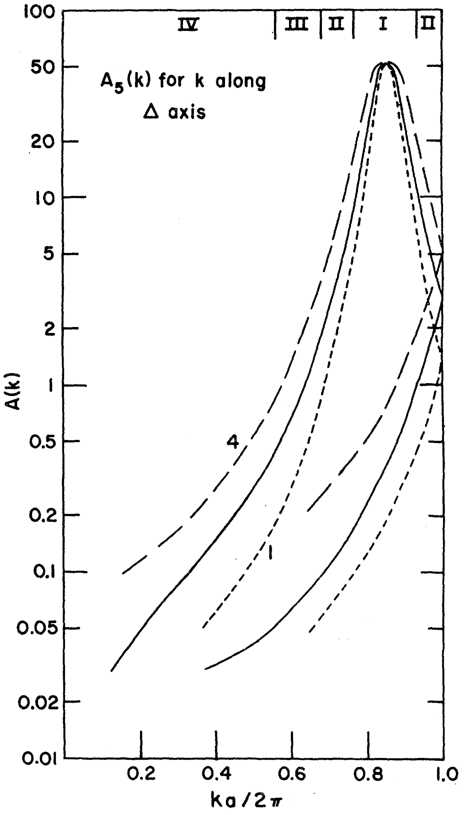

FIG. 16. Plot of $A_n(\vec{k})$ for phosphorous vs $\vec{k}$ for the two lowest conduction bands ($n=5$ and 6) along the Δ axis characterized by $\vec{k}=(2\pi/a)$ $(\delta, 0, 0)$, with $0 \leq \delta \leq 1$. The solid line is the calculated $A_n(\vec{k})$. The dashed line labeled 1 is the Fourier transform of the Whittaker-type function $F(r)$ given by Eq. (27) and is the same as curve 1 in Fig. 3. The dashed line labeled 4 is the transform of the anisotropic EMT solution $F(\vec{r})$ as given by Eq. (30) and is the same as curve 4 in Fig. 3.

Figure 17 shows similar plots of the magnitude of $A_n(\vec{k})$ for phosphorous along directions perpendicular to the Δ axis and passing through the (calculated) conduction-band minimum. The complete shallow-donor problem does not have the cylindrical symmetry about the Δ axis that the EMT assumes. Therefore, the direction perpendicular to the Δ axis must be specified, and plots are shown for directions in the (100) and (110) planes of the Brillouin zone.

In both Figs. 16 and 17 it is observed that the calculated $A_n(\vec{k})$ lie between lines 1 and 3 or 4. This means that anisotropy effects similar to those of the EMT are also present in our final wave function. One might ask whether or not additional reiterations of the $A_n(\vec{k})$ calculation might

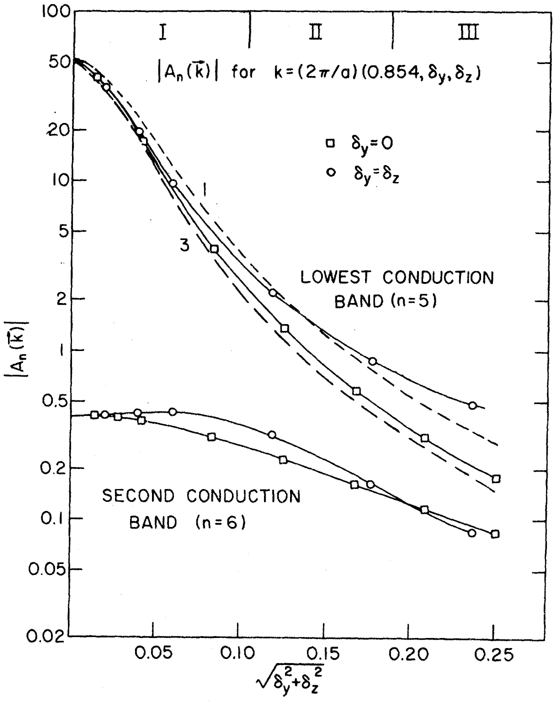

FIG. 17. Plot of $|A_n(\vec{k})|$ for phosphorous vs $\vec{k}$ for the two lowest conduction bands ($n=5$ and 6) along directions perpendicular to the Δ axis through the conduction band minima. The $\vec{k}$ values are characterized by $\vec{k}=(2\pi/a)$ $(0.854, \delta_y, \delta_z)$. The solid lines give the calculated values for two different perpendicular directions: $\delta_y=0$ and $\delta_y=\delta_z$. The dashed curve labeled 1 is the transform of the $F(r)$ given by Eq. (27) and is the same as curve 1 in Fig. 3. The dashed curve labeled 3 is the transform of the anisotropic EMT solution $F(\vec{r})$ as given by Eq. (30) and is the same as curve 3 in Fig. 3.

move closer to the EMT lines 3 and 4. We believe not because in Fig. 17 one observes that the difference between the calculated $A_n(\vec{k})$ for different directions perpendicular to the axis is as great as the difference between the $\delta_y = 0$ line and line 3. Also, since our wave function provides much better agreement with experiment, one should use our calculated $A_n(\vec{k})$ as the standard with which to compare features of the EMT and not vice versa.

Figure 18 shows the real and imaginary parts of $A_n(\vec{k})$ for phosphorous for the same $\vec{k}$ values as for the $\delta_y = \delta_z$ line of Fig. 17. The imaginary component of $A_n(\vec{k})$ is a significant departure from the results of the EMT approximations. The complex nature of $A_n(\vec{k})$ results from the matrix elements $(n\vec{k}|U_p^s(r)|n_0\vec{k}_0)$ [see Eq. (15)] which have complex values when $\vec{k}$ is not in one of the planes $k_x = 0$, $k_y = 0$, or $k_z = 0$. Note that the magnitude of the imaginary part of $A_5(\vec{k})$ of the first conduction band is larger than the magnitude of $A_6(\vec{k})$ of the second conduction band. Note also that the Roman numerals at the top of Figs. 16–18 indicate the regions of k space that were so labeled in Figs. 4 and 5. This indicates that all of the $A_n(\vec{k})$ values shown are making significant contributions to the a_l values. It is the imaginary part of $A_n(\vec{k})$ that is responsible for the lack of inversion symmetry in a_l predictions for the even-numbered sites such as (4, 4, 4) and (4, 4, $\bar{4}$) that are related by inversion. This feature is observed in the experimental a_l values but it is missing in the EMT.

The cellular parts of the Bloch functions $u_n(\vec{k}, \vec{r})$ have been phased to be real at the even-numbered lattice sites. Figure 19 shows a plot of the cellular part of the Bloch function at the lattice sites, $u_n(k, \vec{R}_l)$ for $\vec{k}$ along the Δ axis for the two lowest conduction bands. [The small difference (they should be equal) between $u_5(k, \vec{R}_l)$ and $u_6(k, \vec{R}_l)$ for $\vec{k}$ at the zone boundary is due to the finite set of plane waves used in the calculation. The contribution to the error due to this small difference is negligible.] The variation of $u_n(\vec{k}, \vec{R}_l)$ near the conduction-band minimum is rather slow (the EMT assumes there is no variation). The rapid changes for $\delta < 0.5$ are due to the changing atomic character of the Bloch function. However, this point is not responsible for much of the difference between this work and EMT because the values of $A_n(\vec{k})$ are small (see Fig. 16) in this region and because this region is about one quarter of the total volume of the Brillouin zone (i.e., it is only part of region IV in Fig. 4).

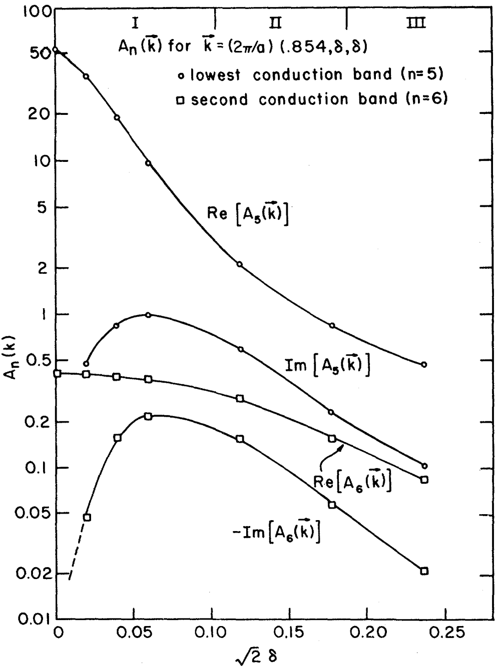

FIG. 18. Plot of the real and imaginary parts of the complex $A_n(\vec{k})$ for phosphorous along a [011] direction through k_0 and perpendicular to the Δ axis.

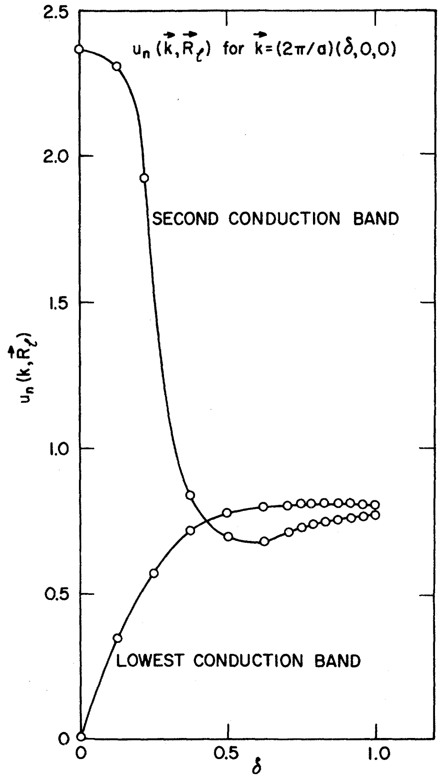

FIG. 19. Plot of the cellular part of the Bloch function at a nuclear site, $u_n(k, \vec{R}_l)$, along the Δ axis.

In addition to the complex nature of $A_n(\vec{k})$ another important difference between this calculation and the EMT occurs for the odd-numbered basis sites. Even though the cellular part of the Bloch functions $u_n(\vec{k}, \vec{r})$ used in this calculation were phased to be real at the even-numbered lattice sites, for a general $\vec{k}$ vector the cellular part of the odd-numbered basis sites, $u_n(\vec{k}, \vec{R}_B)$, is complex. Figure 20 shows plots of $u_5(\vec{k}, 0)$, $u_5(\vec{k}, \vec{R}_B)$, $u_6(\vec{k}, 0)$ and $u_6(\vec{k}, \vec{R}_B)$ for the $\delta_y = \delta_z$ direction perpendicular to the Δ axis. Of course, the magnitudes of $u_n(\vec{k})$ are equal at all lattice sites, i.e., $|u_n(\vec{k}, 0)| = |u_n(\vec{k}, \vec{R}_B)|$ and the differences are due to phase. Note that whereas the magnitudes do not change very rapidly (they are assumed to be constant in the EMT) the phase of $u_n(\vec{k}, \vec{R}_B)$ does change rapidly in regions of k space that make important contributions to the total wave function.

Therefore, we see that the magnitudes of our calculated $A_n(\vec{k})$ are similar to $A(\vec{k})$ of the EMT with similar effective-mass-type anisotropies and that the magnitude of $u_5(\vec{k}, \vec{R}_l)$ does not vary rapidly for $\vec{k}$ values near the conduction-band minima, just as assumed in EMT. Furthermore, we see that the significant differences between our present calculation and EMT are (i) the complex values of $A_n(\vec{k})$ for $\vec{k}$ values not in the (100) planes of k space, and (ii) the complex values of $u_n(\vec{k}, \vec{R}_B)$, the cellular part of the Bloch function at the basis lattice sites.

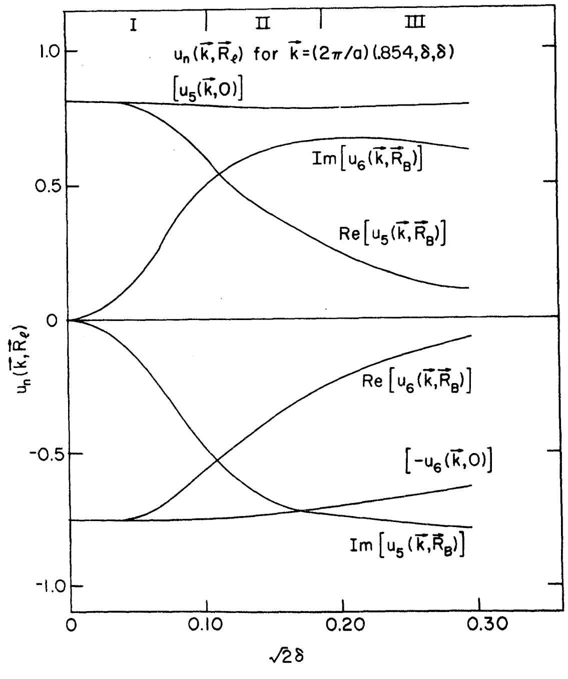

FIG. 20. Plot of the cellular part of the Bloch function at nuclear sites, $u_n(k, \vec{R}_l)$, along a [011] directions through k_0 and perpendicular to the Δ axis. The cellular part of the Bloch functions have been phased to be real at the face centered cubic sites but they are in general complex at the basis sites.

In Eq. (44) we defined an "interpolation envelope function," F_j^C, that is similar to the EMT envelope function. Since F_j^C is complex, we tabulated it in Table II as (F_j^R, F_j^I) for the lattice sites $\vec{R}_l$. One observes that the real parts F_j^R are similar to the corresponding EMT envelope function values F_j which are also tabulated in Table II. However, it should be kept in mind that in Eq. (44) both $A_n(\vec{k})$ and $e^{i\vec{k}\cdot\vec{r}}$ are complex and for the odd-numbered or basis sites $u_n(\vec{k}, \vec{R}_B)$ is in general complex. Therefore, there are also contributions to F_j^R from the imaginary parts of these three complex terms.

We discussed above that setting $G = 0$ in Eq. (46) did not change the a_l values very much. However, when the imaginary part of the "envelope function," F_j^I is also set equal to zero the resulting a_l values (tabulated in column 5 of Table I) are very different and the rms error increases to 38.8%, almost as bad as the EMT results. Therefore, we must conclude that, if we choose to rewrite Eq. (42) in the envelope function form of Eq. (46), then the imaginary part of F_j^C is very important. *This means that no* EMT *approach that is based on a real-valued effective-mass Hamiltonian will ever yield* a_l *values as accurate as we report here.*

Since there has recently been a renewed interest[2,8,9,38-40] in various effective-mass approaches to shallow-donor problems, we shall close this section on comparison of our results with EMT with a few comments on possible future calculations. It is clear from our work that to obtain about 10% accuracy for the a_l values it is important to (a) make a $\vec{k}$-space expansion and (b) use a potential that gives the experimental ionization energy. A possible next step would be to repeat the calculations here with a more "first-principles" choice of donor core potential than the model potential that we have used. However, since we have seen that our results (at the 10% level of accuracy) are not very sensitive to small changes in the shape of the $U(r)F(r)$ product as long as the correct energy is obtained, even a "first-principles" potential that gave the correct energy would probably not significantly change the rms error in the a_l values unless the numerical accuracy of the calculations is improved by using a finer grid in $\vec{k}$ space and by reiterating the $A_n(\vec{k})$ values (or diagonalizing the energy matrix). What is certainly apparent is that no "first-principles" potential in a calculation using just the effective-mass approach will give much better results than the EMT values that are listed in Table I. This is because the details of the $\vec{k}$-space calculation are more important than the details of the potential that one uses in an EMT calculation.

To make a detailed $\vec{k}$-space calculation with 1% numerical accuracy would require three or four orders of magnitude more computer time than we have used in this work. Within a few years sufficient computer speed and capacity will probably be available to make such calculations possible. With 1% numerical accuracy details of "first-principles" core potentials and lattice relaxation will undoubtably become important to the a_l values. Probably around 1% accuracy many other considerations such as exchange polarization effects, limitations of pseudopotential Bloch function, etc., will become important. Since the experimental a_l values can be determined to 0.1% or better accuracy, the hyperfine interaction of the shallow donors will continue for several years to be a challenge to theoretical ingenuity and computer capacity.

V. CONCLUSION

We have calculated the wave function of the $1s(A_1)$ ground state for the three shallow donors P, As, and Sb. This wave function is expressed as an expansion in terms of Bloch functions throughout the Brillouin zone for several energy bands. Using this wave function we have calculated the Fermi-contact interactions for the Si^{29} lattice nuclei and have compared these theoretical values with the experimental values. This comparison has permitted for the first time the assignment of all the experimental ENDOR lines to specific lattice sites near the donors.

The most important differences between our new wave function and the well-known effective-mass wave function appear to be the complex values of the $A_n(\vec{k})$ expansion terms and the complex value of the cellular part of the Bloch function at the basis sites, $u_n(\vec{k}, \vec{R}_B)$.

The average value of the rms percentage error Δ for 63 independent a_l values is 11.2% (compared to 60.8% for the EMT a_l predictions). The results are not improved by variations in the quantities η, ϵ_0, and k_0, whose values are not exactly known, and our best results always correspond to the "accepted" values of these terms. Also, our results are not sensitive to small changes in the shape of our starting envelope function $F(r)$ as long as the model potential is adjusted to give the experimental ionization energy. This indicates that the remaining error is due to a combination of the physical and numerical approximations used in this calculation. A much more difficult calculation that includes more sophisticated potentials, more points in the k-space grid, and some sort of numerical reiteration will be necessary to significantly lower Δ to say 1%. There are still several features of the experimental data that will require such an accuracy to be satisfactorily explained.

Therefore, although we are pleased that we have achieved our original goal of "understanding" the experimental data, we believe that still more accurate calculations will produce additional interesting physical details about the shallow donors in silicon.

---

*Work partially based upon the Ph.D. thesis of J. L. Ivey, Purdue University, 1971 (unpublished). That work supported by the National Science Foundation Grant No. GP15799.

†National Academy of Sciences-National Research Council Post-Doctoral Resident Research Associate.

[1] W. Kohn, *Solid State Physics*, edited by F. Seitz and D. Turnbull (Academic, New York, 1957), Vol. 5.

[2] R. A. Faulkner, Phys. Rev. 184, 713 (1969).

[3] G. Feher, Phys. Rev. 114, 1219 (1959).

[4] E. B. Hale and R. L. Mieher, Phys. Rev. 184, 739 (1969).

[5] E. B. Hale and R. L. Mieher, Phys. Rev. 184, 751 (1969).

[6] E. B. Hale and T. G. Castner, Jr., Phys. Rev. B 1, 4763 (1970).

[7] E. B. Hale and R. L. Mieher, Phys. Rev. B 3, 1955 (1971).

[8] T. G. Castner, Jr., Phys. Rev. B 2, 4911 (1970).

[9] T. H. Ning and C. T. Sah, Phys. Rev. B 4, 3468 (1971).

[10] A brief report of this work appears in J. L. Ivey and R. L. Mieher, Phys. Rev. Lett. 29, 176 (1972).

[11] J. Hermanson and J. C. Phillips, Phys. Rev. 150, 652 (1966).

[12] W. A. Harrison, *Pseudopotentials in the Theory of Metals* (Benjamin, New York, 1966).

[13] D. Brust, Phys. Rev. 134, A1337 (1964).

[14] M. L. Cohen and T. K. Bergstresser, Phys. Rev. 141, 789 (1966).

[15] L. Saravia and D. Brust, Phys. Rev. 171, 916 (1968).

[16] R. A. Faulkner, Phys. Rev. 175, 991 (1968).

[17] J. Callaway and A. J. Hughes, Phys. Rev. 156, 860 (1967).

[18] V. Heine and I. Abarenkov, Philos. Mag. 9, 451 (1964).

[19] A. O. E. Animalu, technical reports, Cavendish Laboratory, 1965 (unpublished).

[20] R. L. Aggarwal and A. K. Ramdas, Phys. Rev. 140, A1246 (1965).

[21] W. Kohn and J. M. Luttinger, Phys. Rev. 97, 883 (1955).

[22] D. R. Penn, Phys. Rev. 128, 2093 (1962).

[23] H. Nara, J. Phys. Soc. Jpn. 20, 778 (1965).

[24] H. Nara and A. Morita, J. Phys. Soc. Jpn. 21, 1852 (1966).

[25] G. Srinivasan, Phys. Rev. 178, 1244 (1969).

[26] J. P. Walter and M. L. Cohen, Phys. Rev. B 2, 1821 (1970).

[27] C. D. Salberg and J. J. Villa, J. Opt. Soc. Am. 47, 244 (1957).

[28] M. Cardona, W. Paul, and H. Brooks, J. Phys. Chem. Solids 8, 204 (1959).

[29] P. Löwdin, J. Chem. Phys. 19, 1396 (1951).

[30] R. A. Faulkner (private communication).

[31] See Ref. 6 for a discussion of various determinations of this value.

[32] We are indebted to K. L. Andrew of Purdue University for his furnishing us a copy of this program.

[33] R. Shulman and B. Wyluda, Phys. Rev. 103, 1127 (1956).

[34] D. K. Wilson, Phys. Rev. 134, A265 (1964).

[35] W. A. Harrison, *Solid State Theory* (McGraw-Hill, New York, 1970).

[36] Shells A through X were used in Eq. (47) except for shell E. Shell E was omitted since the error of both this work and the EMT is large for shell E and since the a_l of the nearest-neighbor shell may well be strongly influenced by such things as lattice relaxation that probably have a weaker influence on most of the other shells.

[37] The J shell has [111] symmetry and thus does not have a first-order shift under a [001] stress.

[38] S. Pantelides and C. T. Sah, Solid State Commun. 11, 1713 (1972).

[39] S. Pantelides, Ph.D. thesis (University of Illinois, 1973) (unpublished).

[40] D. Schechter, Phys. Rev. B 9, 1751 (1974).